Histone acetylation dynamics modulates chromatin conformation and allele-specific interactions at oncogenic loci

Stephanie Sungalee, Yuanlong Liu, Ruxandra Lambuta, Natalya Katanayeva, Maria Donaldson Collier, Daniele Tavernari, Sandrine Roulland, Giovanni Ciriello, Elisa Oricchio

Histone acetylation dynamics modulates chromatin conformation and allele-specific interactions at oncogenic loci

Stephanie Sungalee [1,2,7], Yuanlong Liu[2,3,4,7], Ruxandra A. Lambuta[1,2], Natalya Katanayeva [1,2], Maria Donaldson Collier[1,6], Daniele Tavernari [2,3,4], Sandrine Roulland[5], Giovanni Ciriello [2,3,4] and Elisa Oricchio [1,2] ✉

In cancer cells, enhancer hijacking mediated by chromosomal alterations and/or increased deposition of acetylated histone H3 lysine 27 (H3K27ac) can support oncogene expression. However, how the chromatin conformation of enhancer–promoter interactions is affected by these events is unclear. In the present study, by comparing chromatin structure and H3K27ac levels in normal and lymphoma B cells, we show that enhancer–promoter-interacting regions assume different conformations according to the local abundance of H3K27ac. Genetic or pharmacological depletion of H3K27ac decreases the frequency and the spreading of these interactions, altering oncogene expression. Moreover, enhancer hijacking mediated by chromosomal translocations influences the epigenetic status of the regions flanking the breakpoint, prompting the formation of distinct intrachromosomal interactions in the two homologous chromosomes. These interactions are accompanied by allele-specific gene expression changes. Overall, our work indicates that H3K27ac dynamics modulates interaction frequency between regulatory regions and can lead to allele-specific chromatin configurations to sustain oncogene expression.

Cancer cells modify their epigenome to establish and maintain oncogenic transcriptional programs. Mutations affecting the activity of epigenetic modifiers are common in multiple tumor types, contribute to changing the landscape of DNA methylation and histone post-translational modifications[1], and influence chromatin organization[2–6]. The three-dimensional (3D) structural organization of chromatin is determined, on one side, by the binding of architectural proteins (CTCF and cohesin) that mediate dynamic extrusion and formation of loop domains and, on the other side, by the acquisition of histone post-translational modifications, which contribute to segregating the chromatin into compartments and subcompartments[7–9]. The broad distinction into A and B compartments discriminates between chromatin regions enriched, respectively, for active or inactive histone marks[10,11].

In cancer cells, changes in DNA methylation can reduce DNA binding by chromatin architectural proteins, such as CTCF, favoring the formation of spurious interactions between previously insulated regions, and enabling oncogene expression[2,3]. Mutated chromatin modifiers can alter the distribution of histone marks across the genome[1] and, more specifically within topologically associating domains[4]. In addition to somatic mutations and epigenetic changes, tumor development is accompanied by the acquisition of chromosomal alterations that cause the rearrangements of coding and noncoding regions.

Enhancers are distal noncoding regulatory sequences that control gene expression by interacting with gene promoters[12]. In cancer cells, copy-number alterations, chromosomal translocations and extrachromosomal DNA containing enhancer regions can promote the formation of aberrant enhancer–promoter interactions and transcriptional activation of oncogenes[13–16]. However, oncogenic enhancer activity can also be observed in the absence of chromosomal alterations, and it is associated with the increase and/or spreading of H3K27ac at enhancer regions[17,18]. The ability of enhancers to regulate gene expression depends on their epigenetic status[19]: active enhancers are usually marked by H3K27ac and H3K4me1, whereas loss of H3K27ac and gain of H3K27me3 results in poised or repressed enhancers[20]. Thus, changes in H3K27ac correlate with enhancer activity and gene expression.

The transcriptional kinetics of specific genes can be regulated by intrinsic properties of promoters, transcription factor binding and epigenetic status of the enhancers[21–23]. It is interesting that physical interactions between enhancers and promoters create a permissive chromatin conformation that appears to be sufficient to induce gene expression in the absence of lineage-specific transcription factors[24]. However, interactions between enhancers and promoters do not exist in a binary configuration (that is, the interaction either occurs or does not), but they can assume diverse conformations that might influence gene expression[25]. In the present study, we investigated how, in cancer cells, changes in H3K27ac alter chromatin interactions by repositioning enhancer regions across different subcompartments, and by changing local interactions between enhancers and promoters. In addition, we analyzed the effect of enhancer hijacking on chromosomal translocations on genomic regions proximal to the breakpoints. We show that aberrant distribution of H3K27ac contributed to the formation of allele-specific interactions and monoallelic oncogene expression.

[1]Swiss Institute for Experimental Cancer Research, School of Life Sciences, EPFL, Lausanne, Switzerland. [2]Swiss Cancer Center Leman, Lausanne, Switzerland. [3]Department of Computational Biology, University of Lausanne, Lausanne, Switzerland. [4]Swiss Institute of Bioinformatics, Lausanne, Switzerland. [5]Aix-Marseille University, CNRS, INSERM, Centre d'Immunologie de Marseille-Luminy, Marseille, France. [6]Present address: Division of Molecular Pathology, The Netherlands Cancer Institute, Amsterdam, the Netherlands. [7]These authors equally contributed to this work: Stephanie Sungalee, Yuanlong Liu. ✉e-mail: elisa.oricchio@epfl.ch

Results

Repositioning of enhancer regions across subcompartments. The 3D conformation of chromatin and its compartmentalization are closely associated with the presence of histone post-translational modifications[8,26,27]. However, the broad partition into A and B compartments does not fully capture chromatin state diversity and a more refined classification into subcompartments has been shown to better capture this diversity[8,28]. To understand whether and to what extent changes in H3K27ac lead to repositioning of enhancer regions from one subcompartment to another, we integrated H3K27ac chromatin immunoprecipitation sequencing (ChIP–seq) profiles with high-throughput chromatin conformation capture (Hi-C) data in normal B cells at two distinct stages of differentiation[29–31] (that is, germinal center (GC) B cells and lymphoblastoid B cells), and in malignant B cells transformed from GC cells (Fig. 1a). To unbiasedly identify active enhancer regions that underwent H3K27ac changes during B-cell differentiation and oncogenic transformation, we analyzed ChIP–seq data in a cohort of samples including five diffuse large B-cell lymphoma (DLBCL) cancer cell lines, five GC normal primary samples and a large cohort of normal lymphoblastoid B cells isolated from peripheral blood (n = 76). Candidate enhancer regions detected in these samples were matched when they overlapped and condensed in 9,250 matched enhancer regions (MERs), 1,644 of which were classified as representative of these cohorts because they were shared by multiple samples in each cohort (Supplementary Table 1). Multidimensional scaling of H3K27ac signal intensities in the full set of 9,250 MERs segregated samples based on their biological classification and independently of the sample source (Extended Data Fig. 1a). Consistent with the cell of origin of the tumor, the levels of H3K27ac in MERs were more correlated between GC and DLBCL samples than between each of them and normal lymphoblastoid cells (Extended Data Fig. 1b). Next, we integrated ChIP–seq with Hi-C data obtained from two DLBCL cell lines (WSU-DLCL2 and Karpas-422), one GC sample and the lymphoblastoid cells GM12878 (Supplementary Tables 1 and 2). For each Hi-C experiment, we used the Calder algorithm[28] to infer subcompartment domains[7,9], and clustered them into eight subcompartments (four A and four B subcompartments). Subcompartment domains within each chromosome were ranked between 0 and 1 based on the clustering procedure. Subcompartment domains ranked close to 0 corresponded to domains in repressive B subcompartments, whereas ranks close to 1 corresponded to domains in active A subcompartments. Representative enhancer regions of the analyzed cohorts (n = 1,644) were mapped to their corresponding subcompartment domains to assess whether changes in H3K27ac during B-cell differentiation and oncogenic transformation were associated with enhancer repositioning (that is, change of subcompartment and/or domain rank; Fig. 1b). Subcompartment domain ranks in the two DLBCL cell lines were highly correlated and more associated with GC cells than with lymphoblastoid B cells (Extended Data Fig. 1c), consistent with trends observed for H3K27ac profiles (Extended Data Fig. 1b). Importantly, changes in subcompartment domain ranking between each DLBCL cell line and either GC or lymphoblastoid cells were always significantly correlated with H3K27ac fold-changes (Extended Data Fig. 1d,e) and these subcompartment changes were highly consistent between comparisons (Fig. 1c and Extended Data Fig. 1f,g). It is interesting that, among enhancers that moved toward active subcompartments in DLBCL cell lines compared with GM12878 (rank difference >0; Fig. 1c), we found that some of them were in active subcompartments only in lymphoma cells, whereas others were already in active subcompartments in GC B cells (rank difference ~0). This indicated that repositioning events either were specifically associated with the tumorigenic state of cells (tumor-specific repositioning) or reflected the cell of ori- gin of the tumor and stalled cell differentiation (lineage-associated repositioning; Supplementary Table 3).

To explore in more detail the epigenetic status of a subset of these repositioned enhancers, we selected the most extreme repositioning events with respect to the GM12878 cell line (rank difference >0.4 or <−0.4), which were significantly overlapping between the two lymphoma cell lines (Extended Data Fig. 1h). Subcompartment ranks associated with these enhancers clearly distinguished lineage-associated and tumor-specific repositioning. Indeed, lineage-specific repositioned enhancers (n = 9) were in active subcompartments in both lymphoma cell lines and GC cells, whereas they were found in the repressive subcompartments in GM12878 (Fig. 1d). It is interesting that these events included a cluster of enhancers proximal to *BCL6* gene, which is required for GC formation and frequently upregulated in lymphoma cells[32], or other genes involved in hematopoietic differentiation, such as *CHD7* (ref. [33]) or *ZEB2* (ref. [34]) Conversely, tumor-specific repositioned enhancers shifted toward positive (n = 12) or negative (n = 11) subcompartments specifically in lymphoma cells compared with both GM12878 and GC B cells (Fig. 1e-f). Enhancers that were repositioned in active compartments, specifically in tumor cell lines, were found in proximity to cell-cycle regulators, such as *CDC23* and *CDC25B*, the p53 negative regulator *MDM2* and *NKX2* transcription factors, which have been found aberrantly expressed in B-cell lymphoma[35,36]. Differences in subcompartment localization were always associated with changes of H3K27ac at the corresponding enhancer regions (Fig. 1g-i). To further corroborate these results in independent human tumor samples, we generated and analyzed ChIP–seq and Hi-C data from two primary DLBCL patient samples (patient 1 and patient 7), which have been engrafted in immunocompromised animals[37]. As for the lymphoma cell lines, differences in subcompartments compared with GC or GM12878 cells were positively correlated (Extended Data Fig. 1i), and the most extreme repositioning events (rank difference >0.4 or <−0.4) significantly overlapped (Extended Data Fig. 1j). Repositioning of enhancer regions could again be classified in tumor-specific and lineage-associated repositioning events (Fig. 1j and Supplementary Table 3). Importantly, most of the repositioning events observed in either lymphoma cell lines or patient samples were detected in at least two samples (Fig. 1k), with approximately half of them being found already in GC cells (that is, being associated with the cell of origin of the tumor). A notable example among lineage-specific repositioning events, which were shared among all four lymphoma samples, was a cluster of enhancers proximal to the *BCL6* locus (Fig. 1l). These enhancers were found in the most active subcompartment in all tumor samples and GC cells, but not in GM12878, consistent with the presence of H3K27ac at these loci. Overall, changes of H3K27ac during B-cell differentiation or oncogenic transformation were associated with lineage-associated or tumor-specific repositioning of enhancer regions across chromatin subcompartments.

Modulation of EPIs. Enhancers are distant regulatory elements that control gene expression by forming interactions with the cognate gene promoter; these interacting regions can assume different conformations[25]. Hence, we explored the dependency between the amount of H3K27ac at enhancer regions and the formation of enhancer–promoter interactions (EPIs). For this purpose, we focused on the representative enhancer regions (n = 1,644) that we determined in DLBCL, GC and normal lymphoblastoid B cells. First, we used the HiC-DC algorithm[38] to estimate significantly frequent Hi-C contacts between each candidate enhancer region and gene promoters within 2 Mb of that enhancer. In total, HiC-DC tested 69,030 candidate EPIs in each of the six samples (GC, GM12878, two lymphoma cell lines and two primary patient samples) analyzed by Hi-C, and identified between 2,500 and 4,500 significant EPIs in each model (HiC-DC $P < 0.001$; Extended Data Fig. 2a). Significant EPIs were more likely to occur between enhancers and promoters within the same subcompartment domain than

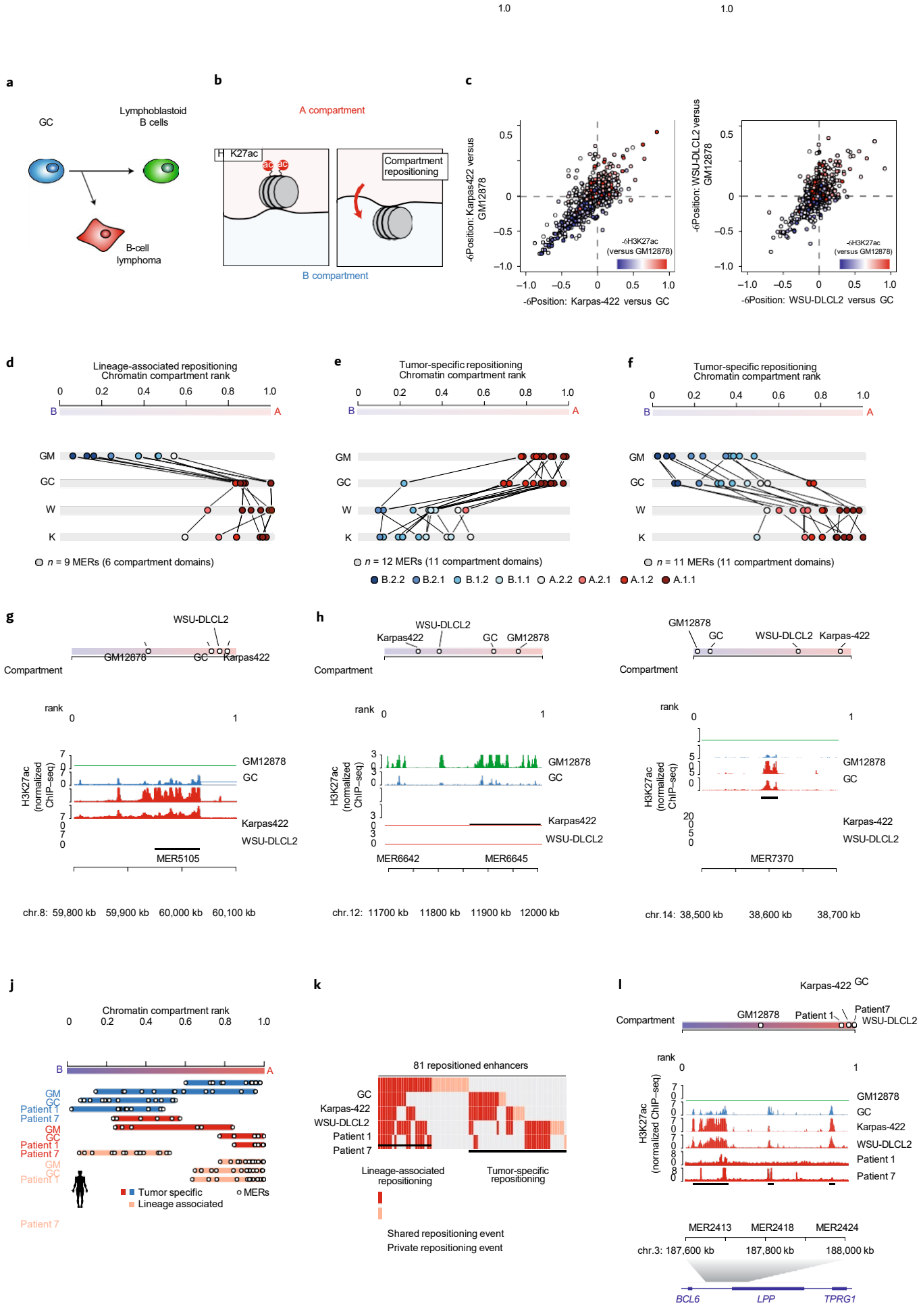

Fig. 1 | Repositioning of enhancer regions in chromatin subcompartment domains. **a**, Graphic representation of the models used in the present study.

Arrows indicate differentiation and tumor development trajectories. **b**, Graphic representation of repositioning of enhancer regions between A and B compartments that accompany changes in H3K27ac. **c**, Comparison of compartment domain rank differences computed with Calder between (left) Karpas-422 and GC cells (*x* axis) and Karpas-422 and GM12878 (*y* axis) and between (right) WSU-DLCL2 and GC cells (x axis) and WSU-DLCL2 and GM12878 (*y* axis). Each dot is an MER color coded by the difference in H3K27ac between Karpas-422 (left) or WSU-DLCL2 (right) and GM12878 (red: higher H3K27ac in lymphoma cell lines than in GM12878; blue: lower H3K27ac in lymphoma cell lines than in GM12878). **d**–**f**, Compartment domain rank (*x* axis) of enhancer regions in cancer cell lines (WSU-DLCL2 (W) and Karpas-422 (K)) and normal B cells (GC and GM12878 (GM)). From left to right: enhancer regions exhibiting lineage-specific repositioning (**d**), and enhancer regions exhibiting tumor-specific repositioning toward inactive (**e**) or active (**f**) subcompartments. Each dot is an enhancer region and color coded by subcompartment assignment. **g**–**i**. Representative examples of H3K27ac ChIP–seq tracks of enhancer regions and their position in the compartment rank in the indicated samples (top bar) indicating lineage associated repositioning on chr.8 (**g**), and tumor specific repositioning chr.12 (**h**) and chr.14 (**i**). **j**, Compartment domain rank (*x* axis) of enhancer regions in lymphoma primary patient samples (patients 1 and 7) and normal B cells (GC and GM12878). **k**, Occurrence of repositioned enhancer regions in the indicated samples compared with GM12878. Shared repositioning events are observed in at least two samples. **l**, H3K27ac ChIP–seq tracks of the indicated region on chr.3 and its position in the compartment rank in the indicated samples. The ChIP–seq scale is reported as normalized reads per million (n.r.p.m.) for cell lines and reference-adjusted reads per million (r.r.p.m.) $\times 10^{-2}$ for patient samples. The position of this region in the larger genomic locus, comprising the *BCL6*, *LPP* and *TPRG1* genes, is shown at the bottom.

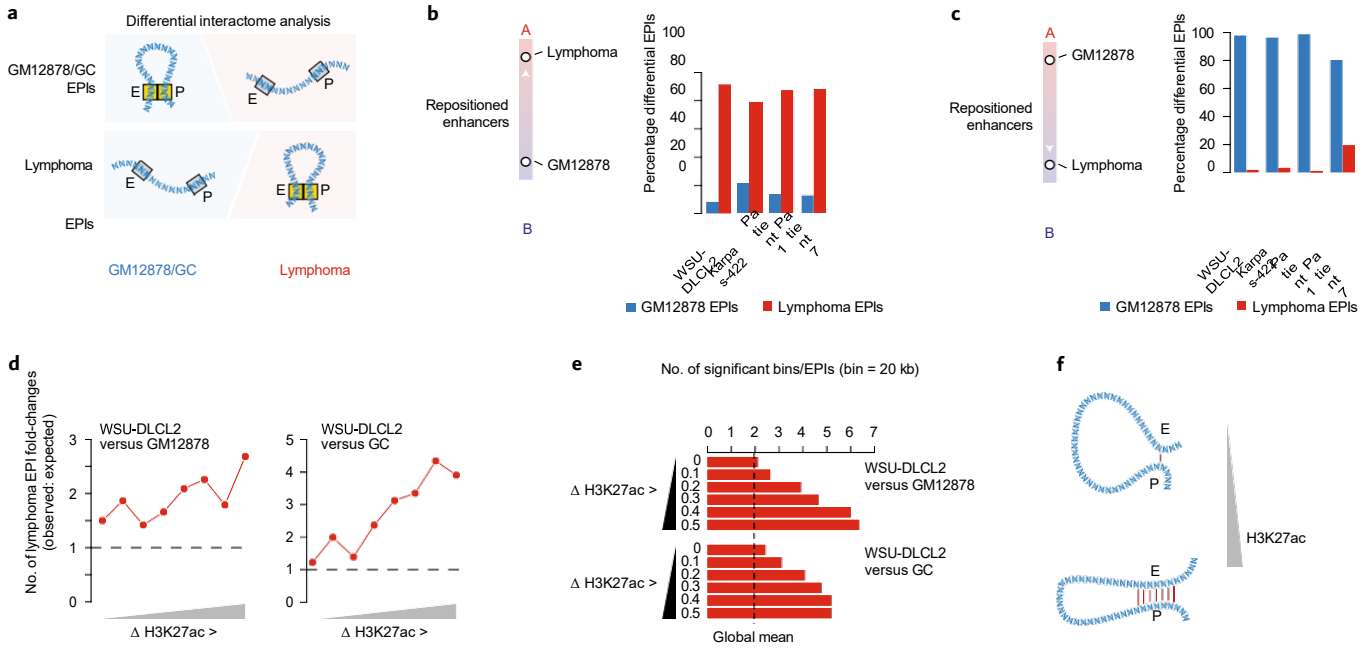

Fig. 2 | Changes in H3K27ac modulate the frequency and size of EPIs. **a**, Graphic representation of the differential interactome analysis. The presence (DNA loop with yellow boxes) and absence (DNA string with gray boxes) of EPIs is compared between normal B cells (GM12878 and GC in blue) and lymphoma cells (red), including both cell lines and primary samples. E, enhancer; P, promoter. **b**,**c**, Percentage of significantly different EPIs (*y* axis), which are more frequent either in GM12878 than in the indicated lymphoma samples (blue bars) or in lymphoma samples than in GM12878 (red bars). Results are shown for enhancer regions that were repositioned from inactive to active compartment (**b**) or from active to inactive compartment (**c**) in lymphoma samples with respect to GM12878. **d**, Fold-change between the observed and expected number of significantly more frequent EPIs (*y* axis) in WSU-DLCL2 than GM12878 (left) and GC (right), with respect to the difference in H3K27ac in these regions. **e**, Number of significant interactions per EPI (that is, number of bins of the Hi-C map with significantly frequent interactions between the enhancer and promoter regions; *x* axis), with respect to the difference in H3K27ac in these regions. Results are shown for EPIs that were more frequent in WSU-DLCL2 than in GM12878 (top) or in GC (bottom). **f**, Graphic representation of the changes in EPI conformation as a consequence of increased H3K27ac considering the number of bins and frequency (represented as red lines) of interactions.

expected (Extended Data Fig. 2b). Next, we performed a differential interactome analysis to estimate significant differences in contact frequency between EPIs in lymphoma cell lines and in normal B cells (GC and GM12878; Fig. 2a and Supplementary Data 1–2). Significantly different EPIs were associated with subcompartment repositioning of enhancer regions. Indeed, the subset of enhancer regions that exhibited the most extreme repositioning (rank difference >0.4 or <-0.4) made significantly more frequent interactions with gene promoters when found in the active subcompartments than when in repressive subcompartments (Fig. 2b,c and Extended Data Fig. 2c). Moreover, the number of significantly different EPIs increased with growing differences of H3K27ac at enhancers (Fig. 2d and Extended Data Fig. 2d). It is interesting that the same trend was observed for the 'size' of interacting regions in these EPIs, defined here as the number of genomic bins that exhibited significant interactions between one enhancer and one promoter (Fig. 2e and Extended Data Fig. 2e). These results indicate that changes of H3K27ac at enhancer regions are associated with EPI formation and that this association is not binary, but the amount of H3K27ac positively correlated with the frequency and size of interactions between enhancer and promoter regions (Fig. 2f).

Depletion of H3K27ac weakens EPIs. To directly assess the effect of histone acetylation on chromatin interactions, we pharmacologically blocked the catalytic activity of the histone acetyltransferases (HATs) p300 and CBP, using the selective small-molecule inhibitor A-485 (ref. [39]) (Fig. 3a). Short-term treatment with A-485 induced genome-wide reduction of H3K27ac in lymphoma cells (Fig. 3a and Extended Data Fig. 2f), but did not affect H3K9ac (Fig. 3a) or significantly influence cell proliferation and survival (Extended Data Fig. 2g). Thus, we performed Hi-C on WSU-DLCL2 and Karpas-422 cells after 48 h of treatment with the A-485 inhibitor (0.5 μM) to test

whether changes in H3K27ac influence EPI formation (Fig. 3b). It is interesting that a decrease of H3K27ac led to an overall loss of chromatin interactions in the A compartment, consistent with H3K27ac enrichment in this compartment, but no differences were found in the B compartment (Extended Data Fig. 2h). Next, we spe- cifically tested the effect of A-485 on EPIs that were found signifi- cantly more frequently in Karpas-422 (n = 239) and WSU-DLCL2 (n = 494) than in lymphoblastoid B cells (Supplementary Table 4). Differential interactome analyses between treated and untreated cells found that the large majority of these EPIs showed a decrease in frequency of interactions (Fig. 3c), including a large fraction of significantly less frequent interactions (45% in Karpas-422 and 68% in WSU-DLCL2). Among EPIs that significantly changed on treat- ment, we found several interactions among enhancers and promot- ers of lymphoma-associated genes, such as *BCL6*, *BCL11A*, *MYC* and *MAP2K1* (Supplementary Table 4), which regulate B-cell dif- ferentiation and tumor cell proliferation. Differential expression analysis between treated and untreated cells showed that less fre- quent EPIs were associated with decreased gene expression in 62.5% (Karpas-422) and 66.5% (WSU-DLCL2) of the cases, and transcrip- tional changes associated with less frequent EPIs often excited a twofold downregulation ($\log_2$(fold-change) < −1) of gene expres- sion (Fig. 3d and Supplementary Table 5). Downregulated genes as a result of EPI loss included oncogenic loci relevant to lymphoma pathogenesis, such as *BCL6*, *BCL11A* and *MYC* (Fig. 3d). Hence, we decided to use these regions for in-depth and high-resolution analyses aimed at defining the consequences of changing H3K27ac on the chromatin structure.

H3K27ac abundance shapes the conformation of EPIs. BCL11A is a zinc finger protein that negatively controls the expression of fetal hemoglobin in erythroid cells[40,41]. In non-Hodgkin's lymphoma, the

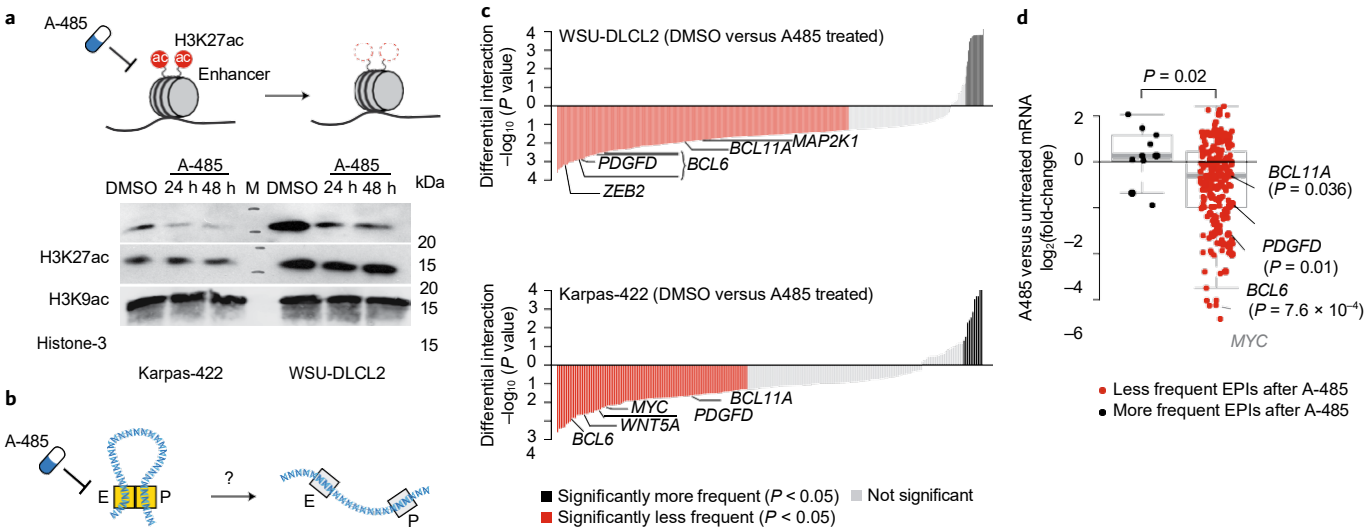

Fig. 3 | Reduction of H3K27ac modulates the frequency and the size of EPIs. **a**, Graphic representation of experimental design on treatment with A-485 inhibitor (top) and a representative western blot image ($n = 2$ independent experiments) detecting the indicated histone post-translational modifications and histone H3 in Karpas-422 and WSU-DLCL2 treated with dimethylsulfoxide (DMSO; vehicle) or A-485 (0.5 μM) for 24 h and 48 h (bottom). **b**. Graphic representation of EPI comparison before and after A-485 treatment. A-485 treatment is hypothesized to induce loss of EPIs. E, enhancer; P, promoter. **c**, Differential interactome significance (*y* axis) of EPIs before and after A-485 treatment: EPIs were either significantly (DiffInt $P < 0.05$) more frequent (black) or less frequent (red) on treatment with A-485 or similarly frequent (not significant—gray) in WSU-DLCL2 (top) and Karpas-422 (bottom). **d**, The mRNA expression fold-changes between A-485-treated and untreated lymphoma cells of genes in which EPIs are less frequent (red) or more frequent (black) on treatment. Fold-changes are computed for both lymphoma cell lines (Karpas-422 and WSU-DLCL2), each analyzed in triplicate. The thick central line in the box plot represents the median value, the bounding box corresponds to the 25th–75th percentiles and the whiskers extend up to 1.5× the interquartile range. Representative genes are labeled. The *P* value was computed using two-tailed Wilcoxon's test.

chr.2p12–16 genomic region, including *BCL11A* and *REL*, is frequently amplified[42,43], and aberrant accumulation of BCL11A in the nucleus has been observed in B-cell malignancies[44]. To understand how *BCL11A* expression is regulated by EPIs in lymphoma, we mapped significant interactions ($q < 0.1$, in a 20-kb bin) between the *BCL11A* promoter and upstream and downstream regions in lymphoma cells. We found multiple bins with significant interactions between *BCL11A* and an upstream H3K27ac-positive enhancer region (chr.2: 60,578–60,584 kb; Fig. 4a and Extended Data Fig. 3a). This represents a lineage-specific enhancer in B cells, because in erythroid cells the expression of *BCL11A* is regulated by a different intragenic enhancer[40,41]. ChIP–seq analyses of H3K27ac in lymphoblastoid B-cell samples, GC samples, lymphoma cell lines and patient samples revealed variable levels of H3K27ac at this enhancer (Extended Data Fig. 3b). The abundance of H3K27ac positively correlated with *BCL11A* expression (Spearman's correlation = 0.75 and $P = 5.8 \times 10^{-14}$) in lymphoblastoid cells (Extended Data Fig. 3c), and with significant overexpression of *BCL11A* in DLBCL compared with lymphoblastoid samples (Extended Data Fig. 3d). Treatment with A-485 reduced H3K27ac in this region (Fig. 4b) and was associated with fewer significant EPIs (Fig. 4b and Extended Data Fig. 3a) and low *BCL11A* expression (Extended Data Fig. 3e). Conversely, the subcompartment domain boundaries and CTCF-binding sites were not affected by treatment with A-485 (Fig. 4a,b and Extended Data Fig. 3f,g), suggesting that the amount of H3K27ac can modulate the EPI frequency, without changing other components of the chromatin architecture. To analyze EPI changes in this region at higher resolution, we performed UMI-4C analyses using bait primers designed on the *BCL11A* enhancer. We confirmed several interactions spanning the region between the enhancer and *BCL11A* beyond specific enhancer–promoter contacts (Fig. 4c).

Treatment with A-485 reduced the overall number of interactions within these regions, but some points of contact between the enhancer (viewpoint) and the region containing the promoter were retained (chr.2: 60.770–60.785 kb) (Fig. 4c). To allay nonspecific

effects due to genome-wide modifications of H3K27ac induced by A-485 treatment, we used an epigenetic, targeted editing approach to modify the acetylation status of the *BCL11A* enhancer. We engineered an independent lymphoma cell line, Su-DHL-4, to constitutively express dCas9 coupled with KRAB, which depletes H3K27ac, and transduced the cells with sgRNAs targeting *BCL11A* enhancer. Only one out of three tested sgRNAs (sgRNA2) signifi- cantly changed *BCL11A* expression (Fig. 4d and Extended Data Fig. 4a) and reduced H3K27ac at the enhancer locus (Fig. 4e and Extended Data Fig. 4b), but it did not affect the acetylation status of flanking regions (Extended Data Fig. 4c). Then, using UMI-4C, we compared the chromatin conformation in cells with and without expression of the sgRNA2. In naive Su-DHL-4 cells, we confirmed frequent interactions within the entire region between the enhancer and *BCL11A* promoter, whereas in cells expressing dCas9–KRAB–sgRNA2 we showed a global reduction in the number of interactions within this region, with only focal points of contact being preserved (Fig. 3f). Next, we tested whether accumulation of H3K27ac in this region could be sufficient to promote the formation of new inter- actions between the *BCL11A* enhancer and promoter. We selected leukemia K562 cells of myeloid origin because they do not express *BCL11A*, and they exhibit neither H3K27ac nor significant EPIs in the region between the enhancer and *BCL11A* (Extended Data Fig. 4d,e). We engineered K562 cells with dCas9–EP300 to pro- mote the deposition of H3K27ac at the *BCL11A* enhancer. In K562 cells expressing dCas9–EP300 with sgRNA2 targeting the enhancer locus, we detected the formation of new interactions in the region between the enhancer and *BCL11A* (Fig. 4g). These changes in chromatin conformation were accompanied by mild accumula- tion of H3K27ac detected by targeted ChIP–quantitative (q)PCR spanning the enhancer locus (Fig. 4h and Extended Data Fig. 4b). Moreover, although *BCL11A* was silenced in K562 cells, we detected low messenger RNA expression of *BCL11A* by both targeted reverse transcriptase-qPCR and RNA-seq in K562 cells engineered with dCas9–EP300–sgRNA2 (Fig. 4i and Extended Data Fig. 4f). These

results demonstrated that ectopic presence of H3K27ac facilitated the formation of de novo interactions within this region and could promote gene expression.

Last, to gain insight on why maintenance of a high level of H3K27ac and multiple EPIs could be beneficial for lymphoma cells, we knocked out *BCL11A* in WSU-DLCL2 cells (Extended Data Fig. 4g). Loss of *BCL11A* expression did not affect lymphoma cell proliferation, but it induced significant downregulation of multiple genes (89% of significantly differentially expressed genes; Fig. 4l and Supplementary Table 6). Geneset enrichment analyses highlighted that several of these genes were regulators of B-cell differentiation, and in particular they were associated with the GC light-zone differentiation[45] (Fig. 4m, Extended Data Fig. 4h and Supplementary Table 6). This suggested that *BCL11A* expression is important in lymphoma cells for stalling B-cell differentiation programs. In-depth analyses of the *BCL11A* locus and associated enhancer indicated that changes of H3K27ac can modulate the interactions in the region between the enhancer and promoter.

H3K27ac effect on EPIs and EEIs. *BCL6* is a key regulator of B-cell maturation in the GC and acts as an oncogene in lymphoma[32]. In GC cells, *BCL6* expression is regulated by a large enhancer region[46] (E1: chr.3: 187,620–187,720 kb) and in lymphoma *BCL6* is constitutively expressed defining the GC origin of these tumors. We compared EPIs at the *BCL6* locus in lymphoblastoid, GC and lymphoma cells. H3K27ac could be detected in the E1 region in GC and lymphoma samples but not in lymphoblastoid samples (Extended Data Fig. 5a). In GM12878, we confirmed lack of H3K27ac at the E1 enhancer and of significant EPIs between the *BCL6* promoter and E1 (Fig. 5a). Conversely, E1–BCL6 interactions were detected in both GC and lymphoma cells (Fig. 5b,c and Extended Data Fig. 5b), in agreement with the enhancer acetylation status in this region. Moreover, in lymphoma cells in which H3K27ac in E1 was higher than in GC cells, additional significant interactions were formed between E1 and multiple downstream H3K27ac peaks (E2, E3, E4) spanning the *LPP* locus, creating a hub of frequently interacting enhancers (Fig. 5c and Extended Data Fig. 5b). A-485 treatment reduced the number of significant interactions with *BCL6* promoter and among the multiple enhancers (Fig. 5d and Extended Data Fig. 5c). Loss of contacts was associated with reduced *BCL6* expression in both lymphoma cell lines (Extended Data Fig. 5d). We used UMI-4C with two independent sets of bait primers, one mapping to E1 and the second to *BCL6* promoter, to analyze at high resolution *BCL6* EPIs and enhancer–enhancer interactions (EEIs). E1 interacted preferentially with *BCL6* promoter and the E2 enhancer, whereas *BCL6* promoter formed multiple interactions with the downstream enhancers (Fig. 5e). Treatment with A-485 reduced the number of interactions in this region, although a few EPIs and EEIs were retained (Fig. 5e). High-resolution chromatin conformation analyses of both the *BCL11A* and *BCL6* loci showed that modulating H3K27ac both changes the frequency of interaction and extends interacting regions among enhancers and between enhancers and promoters.

H3K27ac is necessary to form new EPIs on translocation. In a fraction of DLBCL patients, the region containing E1–E4 enhancers on chr.3 is translocated to chr.8, in proximity to the *MYC* locus[47,48], and it promotes upregulation of *MYC* expression[49]. Hi-C and whole-genome sequencing (WGS) of WSU-DLCL2 cells revealed that these cells harbor a chromosomal translocation t(3:8) between chr.8 and chr.3 (Fig. 5f) similar to the one observed in DLBCL patients. In detail, we detected a copy-number gain containing the large enhancer region on chr.3 (chr.3: 187,481,146–198,295,559 bp), but not including *BCL6*, along with a heterozygote loss of the chr.8 region (chr.8: 129,106,652–139,148,752 bp) downstream of *MYC* (Extended Data Fig. 5e). Copy-number variant analysis showed that the duplicated region of chr.3 was translocated to chr.8, forming a derivative chromosome t(3:8) (Extended Data Fig. 5f), while maintaining the diploid status of the enhancer region regulating *BCL6* in *cis*. Hence, we investigated how changes in H3K27ac affect the chromatin conformation in the translocated chromosome. Using Hi-C, we observed several interactions spanning the chromosomal translocation breakpoint (Fig. 5f) and, by mapping significant interactions in the region, we detected the formation of specific contacts between *MYC* and the chr.3-translocated fragment (Fig. 5g). We confirmed the presence of these new interactions using UMI-4C, in particular between *MYC* promoter and the E1 region on chr.3 proximal to the breakpoint (Fig. 5h). Vice versa, using two independent viewpoints, one on the *MYC* promoter and one on a previously described *MYC* enhancer region[50], and by mapping only intrachromosomal interactions, we could not detect long-range interactions between *MYC* and the chr.8 region beyond the breakpoint (Extended Data Fig. 5g). Treatment with A-485 reduced chr.8–chr.3 (Fig. 5h) and chr.8–chr.8 interactions, while retaining some points of contact with the *PVT1* promoter region (Extended Data Fig. 5g). These changes in interactions were associated with downregulation of *MYC* expression (Fig. 5i). Thus, the formation of new interactions between juxtaposed genomic regions by chromosomal translocation was mediated by H3K27ac (Fig. 5j), and chromatin interactions are instrumental in maintaining oncogene expression.

H3K27ac and allele-specific chromatin conformation. The translocation t(3;8) allows the formation of new interactions between chr.8 and chr.3 mediated by H3K27ac. We asked whether

Fig. 4 | Depletion of H3K27ac modulates the conformation of the *BCL11A* enhancer–promoter loop. **a**,**b**, Representation of 20-kb interacting regions between the indicated genomic coordinates color coded based on their *q* value (top), and the corresponding ChIP–seq track of H3K27ac (r.r.p.m. $\times 10^{-3}$), CTCF (r.p.m.) and CTCF orientation (bottom) in WSU-DLCL2 cells untreated (**a**) and treated with A-485 inhibitor (**b**). **c**, ChIP–seq track of H3K27ac (blue, r.r.p.m. $\times 10^{-3}$) and UMI-4C domainogram representing the mean number of contacts (percentage of the maximum) on the chr.2: 60.4–60.8-Mb region in WSU-DLCL2 cells treated with A-485 (0.5 μM for 48 h) or DMSO as control. **d**, Quantification of *BCL11A* expression changes in Su-DHL-4 cells expressing dCas9–KRAB–sgRNA2 ($n = 6$) compared with the cells expressing dCas9–KRAB (vector, $n = 6$). Data are presented as mean ± s.d. The *P* value was calculated by unpaired, two-tailed Student's *t*-test. **e**, ChIP–seq track of H3K27ac (r.r.p.m. $\times 10^{-3}$) on the chr.2: 60.4–60.8-Mb region in Su-DHL-4 cells expressing dCas9–KRAB (vector) or dCas9–KRAB–sgRNA2. **f**, UMI-4C domainogram representing the mean number of contacts (percentage of the maximum) in Su-DHL-4 cells expressing dCas9–KRAB (vector) or dCas9–KRAB–sgRNA2 with the corresponding H3K27ac (r.r.p.m. $\times 10^{-3}$) ChIP–seq tracks. **g**, ChIP–seq track of H3K27ac (gray, n.r.p.m.) and UMI-4C domainogram representing the mean number of contacts (percentage of the maximum) on the chr.2: 60.4–60.8-Mb region in K562 cells expressing dCas9–EP300 (vector) or dCas9–EP300–sgRNA2. **h**, Quantification with multiple primers spanning the enhancer region (E-p1 to E-p8) of H3K27ac changes in K562 cells expressing dCas9–EP300–sgRNA2 ($n = 3$) compared with the same cells expressing dCas9–EP300 (vector, $n = 3$). Data are presented as mean ± s.d. The *P* values were calculated by unpaired, two-tailed Student's *t*-test. NS indicates $P > 0.1$. **i**, Quantification of *BCL11A* expression changes in K562 cells expressing dCas9–EP300–sgRNA2 ($n = 4$) compared with the same cells expressing dCas9–EP300 (vector $n = 4$). Data are presented as mean ± s.d. j, Volcano plot with differentially expressed genes between *BCL11A* WT and knockout WSU-DLCL2 cells. **l**, Representative example of one of the top scoring genesets containing multiple genes of GC light zone. FDR, false discovery rate; NES, normalized enrichment score.

the presence of a new enhancer region could also influence chr.8–chr.8 chromatin interactions before the breakpoint. Hence, we resolved the chromatin conformation of the two homologous copies of chr.8 before the breakpoint by phasing UMI-4C reads spanning chr.8–chr.8 interactions. To distinguish the chromatin structure of the two chromosomes, first we built the chromosome haplotype based on single-nucleotide polymorphisms (SNPs), then we assigned UMI-4C reads to each copy of chr.8 and pooled reads harboring at least one phased SNP within 20-kb regions (Extended Data Fig. 6a). We confirmed, with two sets of primers (forward and reverse), that all interactions between chr.3 and chr.8 were always supported by only one of the two haplotype blocks (Fig. 6a).

Next, we resolved the chromatin conformation of the regions upstream of the breakpoint in the two chr.8 homologous chromosomes. We independently analyzed reads obtained with multiple bait primers, mapping either to the *MYC* promoter (chr.8: 128,747,000–128,748,470 bp) or to a 60-kb downstream region (chr.8: 128,806,943–128,807,001 bp). The segregation of reads between the two haplotypes revealed that the *MYC* allele on the wild-type (WT) chromosome formed the majority of its interactions

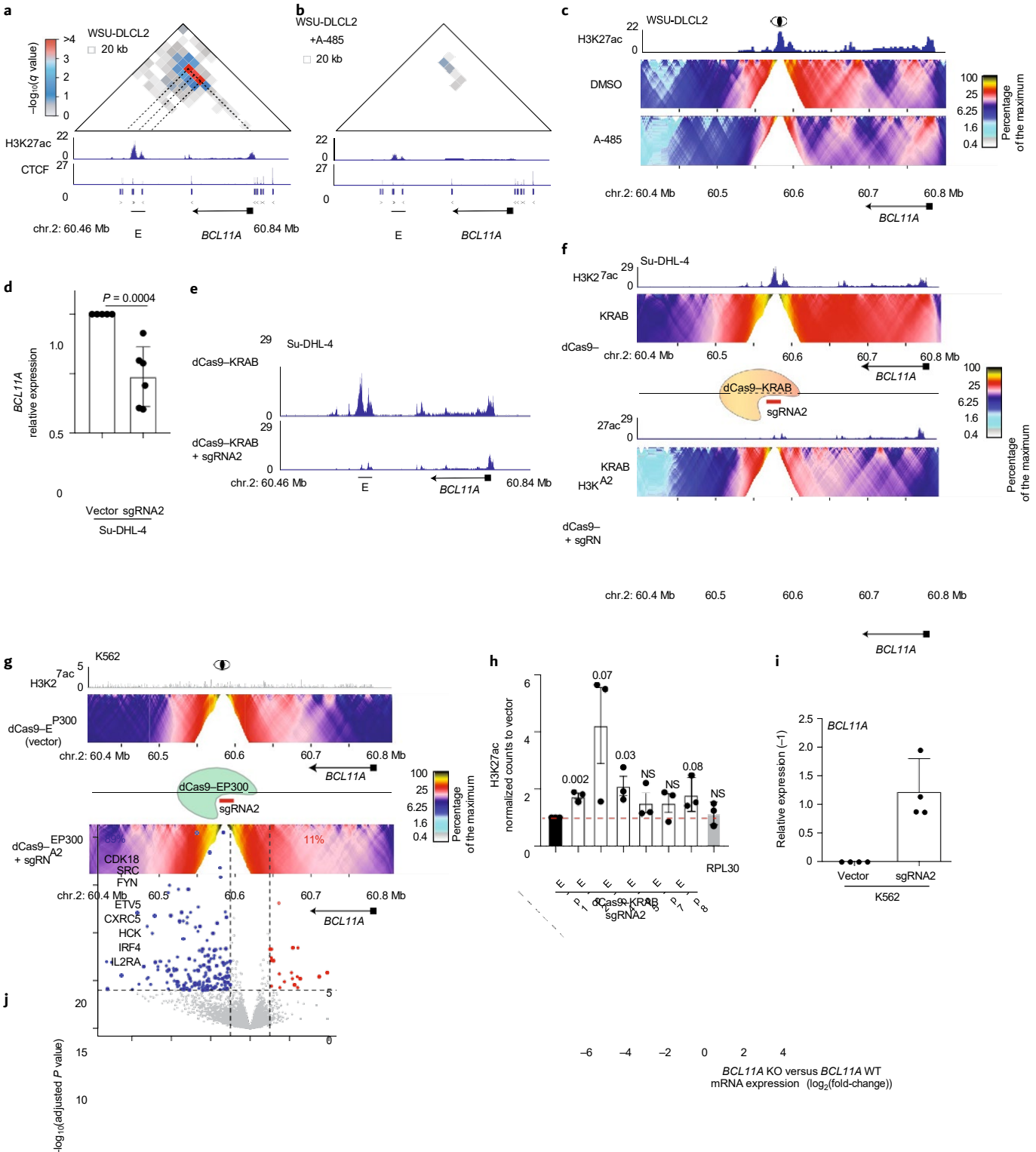

I

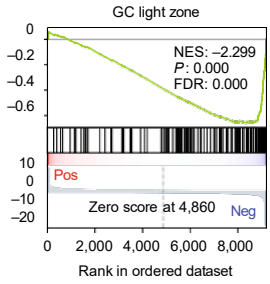

Pos, positively correlated

Neg, negatively correlated

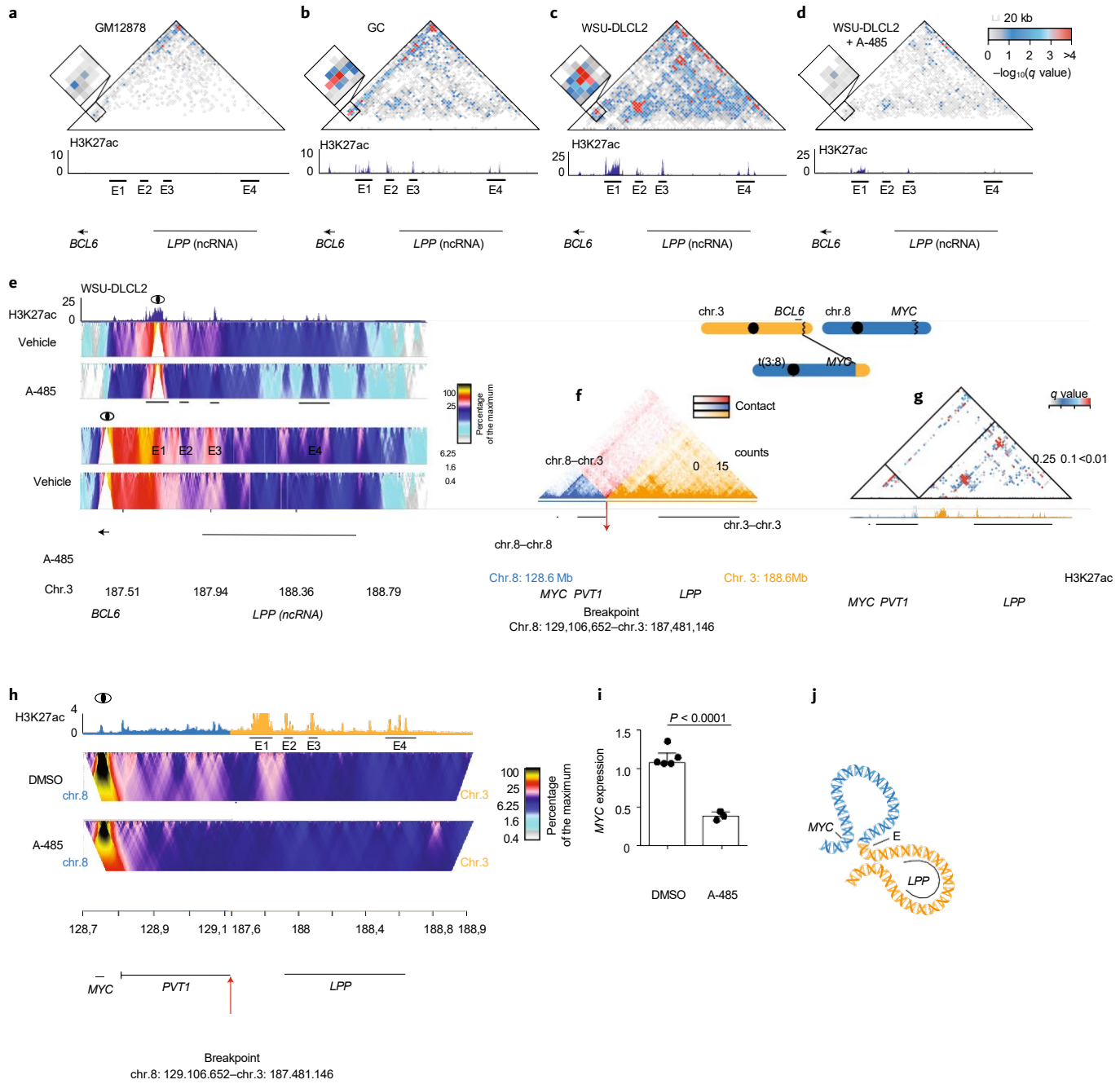

Fig. 5 | Enhancer region on chr.3 regulates the expression of *BCL6* and *MYC*. **a**–**d**, Representation of 20-kb interacting regions between the indicated genomic coordinates with a zoom-in in the region between *BCL6* and E1 enhancer regions (top) and corresponding ChIP–seq track of H3K27ac in GM12878 (n.r.p.m.; **a**), GC (n.r.p.m.; **b**) and WSU-DLCL2 cells untreated (r.r.p.m.; **c**) or treated with A-485 inhibitor (r.r.p.m.; **d**). The 20-kb regions in the interacting maps are color coded based on their *q* value. The enhancer regions detected in lymphoma cells have been labeled with progressive numbers (E1, E2, E3, E4). **e**, The UMI-4C domainogram using two different bait primers and the corresponding H3K27ac ChIP–seq track (r.r.p.m.) in WSU-DLCL2 cells treated with A-485 (0.5 μM for 48 h) or vehicle (DMSO) as a control. The eye represents the position of the primer used as bait. **f**, Graphic representation of the chromosomal translocation t(3:8) between the indicated regions on chr.3 and chr.8, and reconstruction of Hi-C contact maps of the derivative chromosome t(3;8) in the region spanning the breakpoint after chromosomal translocation in WSU-DLCL2. The chr.3 intrachromosomal contacts are in yellow, chr.8 intrachromosomal contacts are in blue and the interchromosomal interactions between chr.3 and chr.8 are in red. **g**, Representation of 20-kb regions significantly interacting color coded based on their *q* values in the derivative chromosome t(3;8) (top) and reconstruction of the H3K27ac ChIP–seq tracks (n.r.p.m.) in WSU-DLCL2 cells (bottom). **h**, UMI-4C domainogram representing the mean number of contacts (percentage of the maximum) spanning the breakpoint after chromosomal translocation between chr.8 and chr.3 in WSU-DLCL2 cells treated with A-485 (0.5 μM for 48 h) or DMSO as control and the corresponding H3K27ac ChIP–seq track in untreated cells. The eye represents the position of the primer used as bait. **i**., Quantification of *MYC* expression changes on treatment with A-485 0.5 μM for 48 h in WSU-DLCL2 ($n = 3$) compared with the same cells treated with DMSO (vehicle $n = 5$). Data are presented as mean ± s.d. The *P* value was calculated using an unpaired, two-tailed Student's *t*-test. **j**, Graphic representation of chromatin conformation on translocation between chr.8 in blue and chr.3 in yellow.

with a genomic region (R1) that is located 160–180 kb downstream of the gene (chr8: 129,020–129,040 kb; Fig. 6b). On the translocated chromosome, *MYC* allele retained interactions observed in the WT allele and formed new specific interactions with a fur- ther distant region (R2) that was 220–240 kb downstream of *MYC* (chr8: 129,100–129,120 kb), in proximity to the breakpoint (Fig. 6c). To

understand whether these differences in chromatin interactions between the two *MYC* alleles could be linked to epigenetic differences between the two chromosomes, we phased H3K27ac ChIP–seq reads. It is of interest that the phasing analysis revealed that H3K27ac was present in the R2 region on the translocated, but not on the WT, chr.8 (Fig. 6d). In addition, we noticed that few H3K27ac peaks proximal to the *MYC* promoter region were exclusively present on the translocated *MYC* allele (Fig. 6d and Extended Data Fig. 6b). Conversely, in other regions upstream of the breakpoint, H3K27ac was similarly distributed between the two copies of chr.8 (Fig. 6d), and also in lymphoma cells (Karpas-422) that do not harbor the t(3;8) translocation (Extended Data Fig. 6c). To

identify regions of preferential interactions with the allele-specific enhancer (asE) at R2, we designed UMI-4C viewpoint primers mapping to the asE region on chr.8 and to the E1 region on chr.3. With these primers, we observed that the asE interacted with E1 on chr.3 and with *MYC* promoter (Fig. 6e). Similarly, the E1 region on chr.3 interacted with both the asE and the *MYC* promoter on chr.8 (Fig. 6e). Thus, the t(3:8) translocation was associated with detection of allele-specific H3K27ac regions on chr.8 and the formation of chr.8–chr.8 allele-specific chromatin interactions.

Last, we observed that *MYC* was expressed exclusively from the translocated allele (Fig. 6f). Indeed, WGS reads mapped to both alleles, whereas 100% of RNA-sequencing (RNA-seq) reads contained the SNP corresponding to the allele on the translocated chromosome, suggesting monoallelic expression of the gene (Fig. 6f). In addition, phasing analysis of ChIP–seq reads showed that H3K36me3, a marker of the transcribed regions, was consistent with phasing of H3K27ac and present only on the *MYC* allele on the t(3:8) chromosome (Fig. 6f and Extended Data Fig. 6b). This was not the case in other regions (Extended Data Fig. 6d,e) or in cells without t(3:8) (Extended Data Fig. 6c–f). Hence, allele-specific chromatin and epigenetic conformation were associated with allele-specific mRNA expression.

Allele-specific conformation and epigenetic changes. Chromosomal translocations involving the highly active immunoglobulin (Ig)H enhancer (IgH-E) region on chr.14 are frequently observed in lymphoma patients[51]. The enhancers on chr.14 are hijacked to boost the expression of oncogenes, such as *MYC* by t(14:8), *BCL6* by t(14:3) or *BCL2* by t(14:18) translocations. In t(14:18), monoallelic expression of the translocated *BCL2* has been reported and it contributes to aberrant upregulation of *BCL2* expression in B-cell malignancies[52]. We detected the translocation t(14:18) in both WSU-DLCL2 cells and patient 1 with the breakpoint in the *BCL2* 3′-UTR region, as described in multiple lymphoma cases[53], whereas this translocation was not present in normal B cells (GC or GM12878) or patient 7 (Extended Data Fig. 7a). Thus, we analyzed how t(14:18) influenced the interactions and H3K27ac profiles of the *BCL2*-translocated and WT allele (Fig. 7a). Similar to what was done for the t(3:8), we reconstructed the Hi-C map of the t(14:18)-translocated chromosome in WSU-DLCL2 and patient 1 (Fig. 7b,c). Several significant interactions were detected between chr.14 and the region including the *BCL2* promoter on chr.18 (Fig. 7d,e). By mapping the corresponding H3K27ac signal, these interactions corresponded to peaks of H3K27ac at the IgH-E region (Fig. 7d,e). Thus, we phased Hi-C and H3K27ac ChIP–seq reads to distinguish between the *BCL2* WT and *BCL2*-translocated t(14:18) alleles in WSU-DLCL2 cells. It is interesting that we observed, in the WT allele, that the region containing the *BCL2* promoter interacted with a region that is 120 kb downstream of the gene (Fig. 7f). Conversely, *BCL2* promoter on the t(14:18) allele formed specific interactions with the *BCL2* 3′-UTR region proximal to the breakpoint (Fig. 7g). As it was observed for the t(3:8) *MYC* locus, allele-specific interactions between *BCL2* promoter and the *BCL2* 3′-UTR region were associated with the presence of an allele-specific H3K27ac signal in this region in both WSU-DLCL2 cells and patient 1 (Fig. 7h). Thus, the *BCL2* promoter of the translocated allele formed specific interactions with the 3′-UTR of the gene, assuming a distinct conformation with respect to the WT allele (Fig. 7i). Overall, in both t(14:18) and t(3:8), the acquired proximity of an enhancer region influenced the epigenetic status and chromatin conformation of the regions proximal to the breakpoints, leading to allele-specific structural, epigenetic and transcriptional profiles.

Discussion

On a broad scale, enrichment for distinct histone marks is associated with A and B compartments, which determine and separate transcriptionally active and inactive chromatin regions[10,54,55]. A more fine-grained description of chromatin compartmentalization revealed subcompartments enriched for distinct histone marks[8]. In transformed cells, hyperacetylation driven by a fusion oncoprotein (BRD4–NUT) was shown to be associated with the formation of a unique subcompartment, suggesting that histone acetylation can promote the formation of new chromatin interactions[26]. In the present study, we showed that differences in H3K27ac between normal and cancer cells correlate with subcompartment repositioning of enhancer regions. Moreover, H3K27ac changes seem to modulate the frequency and extent of contacts between enhancers and their target gene promoters. It appeared that in tumor cells accumulation and spreading of H3K27ac at specific enhancers served to 'zip' these regions in a conformation characterized by increased contact frequency and number of interacting regions, which influence oncogene expression. Importantly, modifications of H3K27ac levels due to chromosomal rearrangements, stalling of cell differentiation, or pharmacological and genetic alterations of HAT activity modify the frequency of interactions of these chromatin structures and can influence gene expression. We observed that, in leukemic cells, the targeted activity of dCas9–EP300 on the enhancer region prompted the formation of chromatin interactions with the proximal gene promoter, but was accompanied by modest changes in gene expression. It is difficult to determine a temporal or causal order among epigenetic, chromatin structure and expression changes. Indeed, it has been shown that direct inhibition of transcription does not necessarily affect chromatin conformation[26]. Moreover, histone-modifying enzymes can affect gene expression through noncatalytic functions[56–58]. Thus, the functional relationship between gene expression and epigenetic modifications is complex and further mechanistic studies are required to explain this dependency.

In cancer, genomic lesions affecting coding regions, such as mutations or chromosomal alterations, have a direct impact on gene expression, whereas chromosomal rearrangements targeting noncoding regions have been associated with enhancer hijacking[13,59]. It is interesting that we found that enhancer hijacking by chromosomal translocations modifies not only interactions between two regions of distinct chromosomes, but also the chromatin conformation

Fig. 6 | Allele-specific epigenetic marks and chromatin interactions at the *MYC* locus. **a**, Number of contacts between one copy on chr.8 (chr.8: 128.6–129.1 Mb) and the chr.3-translocated region detected by UMI-4C using multiple forward (Fwd and F) and reverse (Rev and R) bait primers. The number of reads in 20-kb bins is indicated. **b**,**c**, Number of contacts in the WT chromosome between *MYC* WT (**b**) and translocated allele t(3:8) (**c**; bait primers 1 and 2) and the chr.8: 128.6–129.1-Mb region and number of contacts between a region 60 kb (bait primers 3 and 4) upstream of *MYC* and the chr.8: 128.6–129.1-Mb region. The number of reads in 20-kb bins is indicated. The specific bins are labeled with R1 (region 1) and R2 (region 2). On the right, a graphic representation of the chromosome conformations chr.8 WT or translocated. **d**, H3K27ac ChIP–seq tracks (n.r.p.m.) of the chr.8: 128.6–129.1-Mb regions and the zoom-in of chr.8: 128.73–128.77 Mb and chr.8: 129.04–129.110 Mb. The distribution of the total signal is in gray, the distribution of the signal in the WT chromosome is in blue and the distribution of signal of the translocated chromosome is in red. **e**, UMI-4C domainogram using a bait primer on the asE region (top) and a bait on the E1 region on chr.3 (bottom) representing the $\log_2$(UMI contacts) spanning the breakpoint after chromosomal translocation between chr.8 and chr.3 in WSU-DLCL2 cells, and the corresponding phased H3K27ac ChIP–seq track for chr.8 (r.r.p.m. $\times 10^{-3}$) and total H3K27ac for chr.3 (n.r.p.m.). The eye represents the position of the primer used as bait. **f**, Quantification of the number of reads spanning the chr.8: 128,750,540 SNPs on *MYC* coding region harboring an adenine (A) or a guanine (G) detected by WGS, RNA-seq and ChIP–seq of H3K27ac or H3K36me3 in WSU-DLCL2 cells.

and the epigenetic status of the region proximal to the breakpoint in homologous chromosomes. The presence of allele-specific H3K27ac marks suggested that the translocated enhancer region influenced the epigenetic status and the chromatin conformation of the neighboring region. In nonpathological conditions, multiple genes show allele expression bias across individuals[60,61] and among

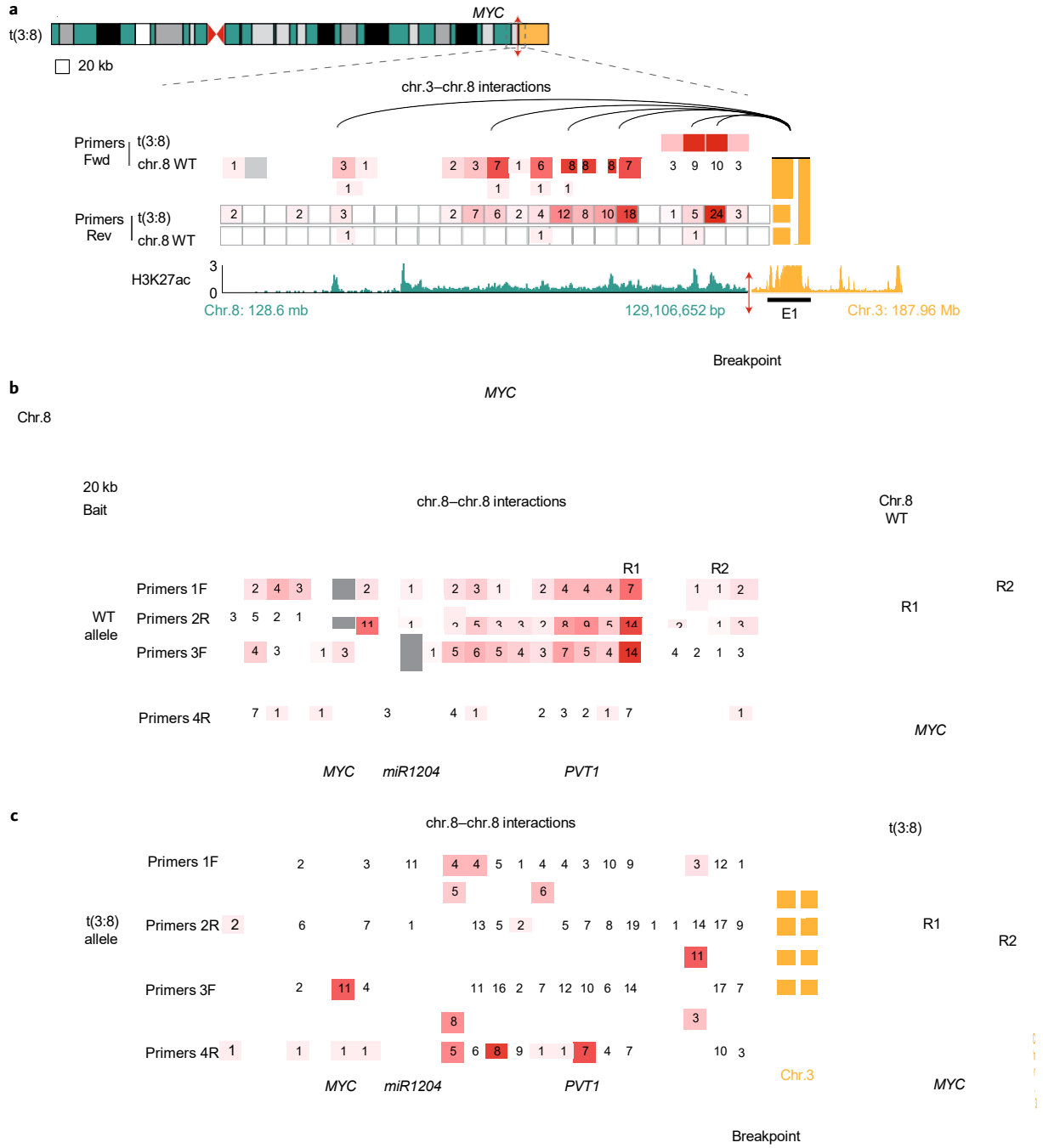

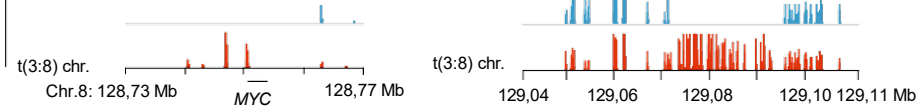

e

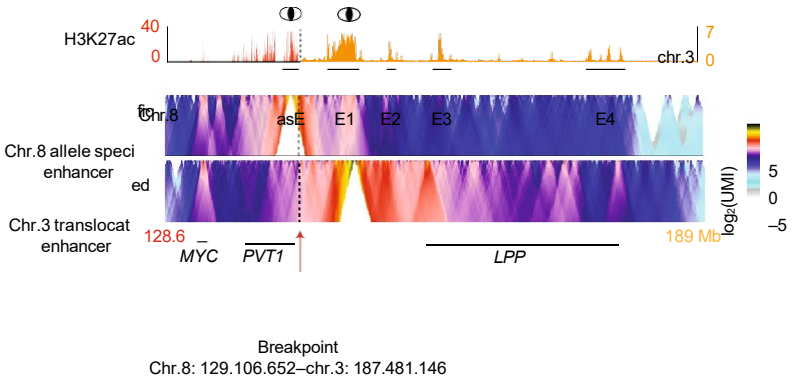

Breakpoint
Chr.8: 129.106.652–chr.3: 187.481.146

f

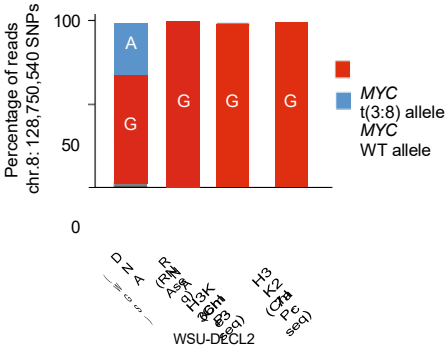

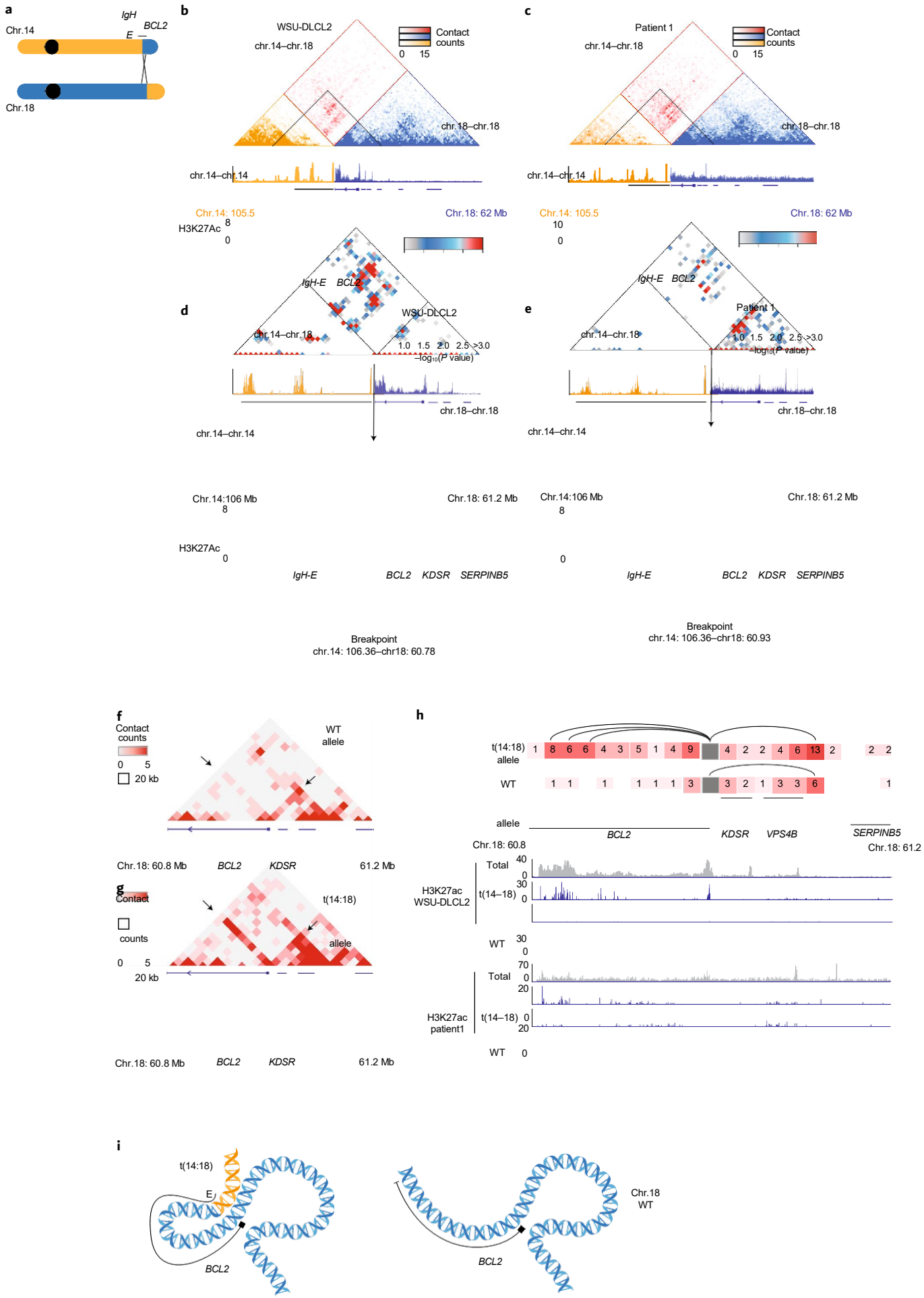
a
IgH
BCL2
E
Chr.14
Chr.18
b
WSU-DLCL2
chr.14–chr.18
Contact counts
0 15
chr.18–chr.18
chr.14–chr.14
Chr.14: 105.5
Chr.18: 62 Mb
H3K27Ac
8
0
IgH-E
BCL2
c
Patient 1
chr.14–chr.18
Contact counts
0 15
chr.18–chr.18
chr.14–chr.14
Chr.14: 105.5
Chr.18: 62 Mb
10
0
IgH-E
BCL2
d
WSU-DLCL2
chr.14–chr.18
1.0 1.5 2.0 2.5 >3.0
−log10(P value)
chr.18–chr.18
chr.14–chr.14
e
Patient 1
chr.14–chr.18
1.0 1.5 2.0 2.5 >3.0
−log10(P value)
chr.18–chr.18
chr.14–chr.14
Chr.14:106 Mb
Chr.18: 61.2 Mb
8
H3K27Ac
0
IgH-E
BCL2
KDSR
SERPINB5
Breakpoint
chr.14: 106.36–chr18: 60.78
Chr.14:106 Mb
Chr.18: 61.2 Mb
8
0
IgH-E
BCL2
KDSR
SERPINB5
Breakpoint
chr.14: 106.36–chr18: 60.93
f
Contact counts
0 5
20 kb
WT allele
Chr.18: 60.8 Mb
BCL2
KDSR
61.2 Mb
g
Contact counts
0 5
20 kb
t(14:18)
allele
Chr.18: 60.8 Mb
BCL2
KDSR
61.2 Mb
h
t(14:18) allele
1 8 6 6 4 3 5 1 4 9 4 2 2 4 6 13 2 2 2
WT
1 1 1 1 1 1 3 3 2 1 3 3 6 1
allele
BCL2
KDSR
VPS4B
SERPINB5
Chr.18: 60.8
Chr.18: 61.2
H3K27ac WSU-DLCL2
Total
t(14–18)
40
0
30
0
WT
30
0
H3K27ac patient1
Total
70
0
20
t(14–18)
0
20
WT
0
i
t(14:18)
E
BCL2
BCL2
Chr.18 WT

Fig. 7 | Allele-specific epigenetic marks and chromatin interactions at the *BCL2* locus. **a**, Graphic representation of the chromosomal translocation t(14:18). **b**,**c**, Reconstruction of Hi-C contact maps of the derivative chromosome t(14;18) in the region spanning the breakpoint after chromosomal translocation in WSU-DLCL2 (**b**) and patient 1 (**c**). The chr.14 intrachromosomal contacts are in yellow, chr.18 intrachromosomal contacts in blue and interchromosomal interactions between chr.14 and chr.18 in red. The dotted lines indicate the region represented in **d** and **e**. **d**,**e**, Representation of 20-kb regions significantly interacting are color coded based on their *P* values in the derivative chromosome t(14;18) and reconstruction of the corresponding H3K27ac ChIP–seq tracks in WSU-DLCL2 cells (n.r.p.m.; **d**) and patient 1 (r.r.p.m. $\times 10^{-2}$; **e**). *P* values obtained with the HiC-DC method are represented. **f**,**g**, Representation of allele-specific Hi-C interactions in the region containing the *BCL2* WT allele and *BCL2*-translocated t(14:18) allele. **h**, Quantification of the Hi-C reads starting from the 20-kb bins containing the *BCL2* promoter in the WT and translocated t(14:18) allele (top) and distribution of H3K27ac ChIP–seq tracks in the corresponding WT and translocated t(14:18) chromosome in WSU-DLCL2 cells and patient 1 (bottom). The H3K27ac distribution of the total signal is in gray. The number of reads in each 20-kb bin is indicated. **i**, Graphic representation of chromatin conformation of *BCL2* WT and translocated alleles on the two copies of chr.18.

different lineages derived from the same stem cells[62]. The unbalanced expression between the two alleles has been associated with a different distribution of histone acetylation and DNA methylation[60,62]. Based on our results, it will be interesting to investigate whether, in these regions, two homologous chromosomes assume a distinct chromatin conformation.

Overall, in cancer cells, beyond chromosomal translocations, other chromosomal alterations such as insertions or heterozygous deletions could induce the acquisition of distinct epigenetic marks and chromatin interactions in the two homologous chromosomes. Disentangling the effects of these alterations on distinct alleles could help explain their oncogenic potential and reveal the emergence of allele-specific configurations as a broad mechanism to deregulate gene expression in cancer cells.

Online content

Any methods, additional references, Nature Research reporting summaries, source data, extended data, supplementary information, acknowledgements, peer review information; details of author contributions and competing interests; and statements of data and code availability are available at https://doi.org/10.1038/s41588-021-00842-x.

Received: 2 May 2020; Accepted: 10 March 2021;
Published online: 10 May 2021

References

1. Feinberg, A. P., Koldobskiy, M. A. & Göndör, A. Epigenetic modulators, modifiers and mediators in cancer aetiology and progression. *Nat. Rev. Genet.* **17**, 284–299 (2016).
2. Flavahan, W. A. et al. Insulator dysfunction and oncogene activation in IDH mutant gliomas. *Nature* **529**, 110–114 (2016).
3. Flavahan, W. A. et al. Altered chromosomal topology drives oncogenic programs in SDH-deficient GISTs. *Nature* **575**, 229–233 (2019).
4. Donaldson-Collier, M. C. et al. EZH2 oncogenic mutations drive epigenetic, transcriptional, and structural changes within chromatin domains. *Nat. Genet.* https://doi.org/10.1038/s41588-018-0338-y (2019).
5. Achinger-Kawecka, J. et al. Epigenetic reprogramming at estrogen-receptor binding sites alters 3D chromatin landscape in endocrine-resistant breast cancer. *Nat. Commun.* **11**, 320 (2020).
6. Viny, A. D. et al. Cohesin members Stag1 and Stag2 display distinct roles in chromatin accessibility and topological control of HSC self-renewal and differentiation. *Cell Stem Cell* **25**, 682–696.e8 (2019).
7. Beagan, J. A. & Phillips-Cremins, J. E. On the existence and functionality of topologically associating domains. *Nat. Genet.* **52**, 8–16 (2020).
8. Rao, S. S. P. et al. A 3D map of the human genome at kilobase resolution reveals principles of chromatin looping. *Cell* **159**, 1665–1680 (2014).
9. Rao, S. S. P. et al. Cohesin loss eliminates all loop domains. *Cell* **171**, 305–320.e24 (2017).
10. Lieberman-Aiden, E. et al. Comprehensive mapping of long-range interactions reveals folding principles of the human genome. *Science* **326**, 289–293 (2009).
11. Dixon, J. R. et al. Topological domains in mammalian genomes identified by analysis of chromatin interactions. *Nature* **485**, 376–380 (2012).
12. Schoenfelder, S. & Fraser, P. Long-range enhancer–promoter contacts in gene expression control. *Nat. Rev. Genet.* **20**, 437–455 (2019).
13. Weischenfeldt, J. et al. Pan-cancer analysis of somatic copy-number alterations implicates IRS4 and IGF2 in enhancer hijacking. *Nat. Genet.* **49**, 65–74 (2017).
14. Koche, R. P. et al. Extrachromosomal circular DNA drives oncogenic genome remodeling in neuroblastoma. *Nat. Genet.* **52**, 29–34 (2020).
15. Morton, A. R. et al. Functional enhancers shape extrachromosomal oncogene amplifications. *Cell* **179**, 1330–1341.e13 (2019).
16. Hnisz, D. et al. Activation of proto-oncogenes by disruption of chromosome neighborhoods. *Science* https://doi.org/10.1126/science.aad9024 (2016).
17. Hnisz, D. et al. Super-enhancers in the control of cell identity and disease. *Cell* **155**, 934–947 (2013).
18. Hnisz, D. et al. Convergence of developmental and oncogenic signaling pathways at transcriptional super-enhancers. *Mol. Cell* **58**, 362–370 (2015).
19. Ernst, J. et al. Systematic analysis of chromatin state dynamics in nine human cell types. *Nature* **473**, 43–49 (2011).
20. Calo, E. & Wysocka, J. Modification of enhancer chromatin: what, how and why? *Mol. Cell* **49**, 825–837 (2013).
21. Andersson, R. & Sandelin, A. Determinants of enhancer and promoter activities of regulatory elements. *Nat. Rev. Genet.* **21**, 71–87 (2020).
22. Bartman, C. R., Hsu, S. C., Hsiung, C. C.-S., Raj, A. & Blobel, G. A. Enhancer regulation of transcriptional bursting parameters revealed by forced chromatin looping. *Mol. Cell* **62**, 237–247 (2016).
23. Larsson, A. J. M. et al. Genomic encoding of transcriptional burst kinetics. *Nature* **565**, 251–254 (2019).
24. Deng, W. et al. Controlling long-range genomic interactions at a native locus by targeted tethering of a looping factor. *Cell* **149**, 1233–1244 (2012).
25. Chen, H. et al. Dynamic interplay between enhancer–promoter topology and gene activity. *Nat. Genet.* **50**, 1296–1303 (2018).
26. Rosencrance, C. D. et al. Chromatin hyperacetylation impacts chromosome folding by forming a nuclear subcompartment. *Mol. Cell* **78**, 112–126.e12 (2020).
27. Bonev, B. & Cavalli, G. Organization and function of the 3D genome. *Nat. Rev. Genet.* **17**, 661–678 (2016).
28. Liu, Y. et al. Systematic inference and comparison of multi-scale chromatin sub-compartments connects spatial organization to cell phenotypes. *Nat. Commun.* https://doi.org/10.1038/s41467-021-22666-3 (2021).
29. Amoli, M. M., Carthy, D., Platt, H. & Ollier, W. E. R. EBV Immortalization of human B lymphocytes separated from small volumes of cryo-preserved whole blood. *Int. J. Epidemiol.* **37**, i41–i45 (2008).
30. Koues, O. I. et al. Enhancer sequence variants and transcription-factor deregulation synergize to construct pathogenic regulatory circuits in B-cell lymphoma. *Immunity* **42**, 186–198 (2015).
31. Zhang, J. et al. The CREBBP acetyltransferase is a haploinsufficient tumor suppressor in B-cell lymphoma. *Cancer Discov.* **7**, 322–337 (2017).
32. Basso, K. & Dalla-Favera, R. Roles of BCL6 in normal and transformed germinal center B cells. *Immunol. Rev.* **247**, 172–183 (2012).
33. Hsu, J. et al. CHD7 and Runx1 interaction provides a braking mechanism for hematopoietic differentiation. *Proc. Natl Acad. Sci. USA* **117**, 23626–23635 (2020).
34. Li, J. et al. The EMT transcription factor Zeb2 controls adult murine hematopoietic differentiation by regulating cytokine signaling. *Blood* **129**, 460–472 (2017).
35. Robles, E. F. et al. Homeobox NKX2-3 promotes marginal-zone lymphomagenesis by activating B-cell receptor signalling and shaping lymphocyte dynamics. *Nat. Commun.* **7**, 11889 (2016).
36. Nagel, S. et al. NKL homeobox gene NKX2-2 is aberrantly expressed in Hodgkin lymphoma. *Oncotarget* **9**, 37480–37496 (2018).
37. Battistello, E. et al. Pan-SRC kinase inhibition blocks B-cell receptor oncogenic signaling in non-Hodgkin lymphoma. *Blood* https://doi.org/10.1182/blood-2017-10-809210 (2018).
38. Carty, M. et al. An integrated model for detecting significant chromatin interactions from high-resolution Hi-C data. *Nat. Commun.* **8**, 15454 (2017).
39. Lasko, L. M. et al. Discovery of a potent catalytic p300/CBP inhibitor that targets lineage-specific tumors. *Nature* **550**, 128–132 (2017).
40. Bauer, D. E. et al. An erythroid enhancer of BCL11A subject to genetic variation determines fetal hemoglobin level. *Science* **342**, 253–257 (2013).
41. Canver, M. C. et al. BCL11A enhancer dissection by Cas9-mediated in situ saturating mutagenesis. *Nature* **527**, 192–197 (2015).
42. Okosun, J. et al. Integrated genomic analysis identifies recurrent mutations and evolution patterns driving the initiation and progression of follicular lymphoma. *Nat. Genet.* **46**, 176–181 (2014).
43. Rao, P. H. et al. Chromosomal and gene amplification in diffuse large B-cell lymphoma. *Blood* **92**, 234–240 (1998).
44. Weniger, M. A. et al. Gains of the proto-oncogene BCL11A and nuclear accumulation of BCL11A XL protein are frequent in primary mediastinal B-cell lymphoma. *Leukemia* **20**, 1880–1882 (2006).
45. Victora, G. D. et al. Identification of human germinal center light and dark zone cells and their relationship to human B-cell lymphomas. *Blood* **120**, 2240 (2012).
46. Bunting, K. L. et al. Multi-tiered reorganization of the genome during B cell affinity maturation anchored by a germinal center-specific locus control region. *Immunity* **45**, 497–512 (2016).
47. Chong, L. C. et al. High-resolution architecture and partner genes of MYC rearrangements in lymphoma with DLBCL morphology. *Blood Adv.* **2**, 2755–2765 (2018).
48. Ohno, H., Nakagawa, M., Kishimori, C., Fukutsuka, K. & Honjo, G. Cryptic t(3;8)(q27;q24) and/or MYC-BCL6 linkage associated with MYC expression by immunohistochemistry is frequent in multiple-hit B-cell lymphomas. *Blood Cancer J.* **7**, e578 (2017).
49. Ryan, R. J. H. et al. Detection of enhancer-associated rearrangements reveals mechanisms of oncogene dysregulation in B-cell lymphoma. *Cancer Discov.* **5**, 1058–1071 (2015).
50. Cho, S. W. et al. Promoter of lncRNA gene PVT1 is a tumor-suppressor DNA boundary element. *Cell* **173**, 1398–1412.e22 (2018).
51. Küppers, R. & Dalla-Favera, R. Mechanisms of chromosomal translocations in B cell lymphomas. *Oncogene* **20**, 5580–5594 (2001).

52. Graninger, W. B., Seto, M., Boutain, B., Goldman, P. & Korsmeyer, S. J. Expression of Bcl-2 and Bcl-2-Ig fusion transcripts in normal and neoplastic cells. *J. Clin. Invest.* **80**, 1512–1515 (1987).
53. Tsujimoto, Y., Cossman, J., Jaffe, E. & Croce, C. M. Involvement of the *bcl-2* gene in human follicular lymphoma. *Science* **228**, 1440–1443 (1985).
54. Boettiger, A. N. et al. Super-resolution imaging reveals distinct chromatin folding for different epigenetic states. *Nature* **529**, 418–422 (2016).
55. Falk, M. et al. Heterochromatin drives compartmentalization of inverted and conventional nuclei. *Nature* **570**, 395–399 (2019).
56. Morgan, M. A. J. & Shilatifard, A. Reevaluating the roles of histone-modifying enzymes and their associated chromatin modifications in transcriptional regulation. *Nat. Genet.* **52**, 1271–1281 (2020).
57. Douillet, D. et al. Uncoupling histone H3K4 trimethylation from developmental gene expression via an equilibrium of COMPASS, Polycomb and DNA methylation. *Nat. Genet.* **52**, 615–625 (2020).

Methods

The present study complies with all ethical regulations. Genetic manipulation of the cell lines was approved from OFSP reference no. A151466/2.

Cell lines, normal GC B cells and patient-derived cells. Lymphoma cell lines WSU-DLCL2, Karpas-422 and K562 were obtained from DSMZ, and Su-DHL-4 and OCI-Ly7 from a previous collaboration. All cell lines were authenticated with short tandem repeat profiling (Microsynth AG). Cell lines were maintained in Gibco RPMI 1640 medium (Thermo Fisher Scientific, catalog no. 61870036) supplemented with 10% Gibco fetal bovine serum (Thermo Fisher Scientific, catalog no. 10270106) and 1% Gibco penicillin–streptomycin (Thermo Fisher Scientific, catalog no. 15140122). Cells were maintained at appropriate densities and propagated in a humidity-controlled, sterile incubator at 37 °C and 5% CO_2. GC B cells isolated from a healthy spleen donor were FACS sorted on an Influx cell sorter using the following antibodies: FITC anti-IgM (314506), APC-Cy7 anti-CD3 (344817), APC-Cy7 anti-CD14 (325619), phycoerythrin (PE) anti-CD10 (312203), PE-Cy7 anti-CD20 (302312) and BV785 anti-CD38 (303529) from BioLegend, and BV421 anti-CD27 (562513), allophycocyanin (APC) anti-IgD (561303) and PE-CF594 anti-CD19 (562294) from Becton Dickinson, and Fixable viability dye eFluor510 (Life Technologies), and then were fixed for Hi-C and ChIP preparation immediately after sorting. The dilution of each antibody was tested and used according to the manufacturer's instructions. Patient 1 (31,357) and patient 7 (13,796) samples were obtained from the Dana-Farber collection and expanded in NOD–SCID (severe combined immunodeficient) animals as described in Battistello et al.[37]. Tumor cells were isolated using a Mouse Cell Depletion Kit (Miltenyi Biotec, catalog no. 130104694). The treatment condition with A-485 inhibitor is reported in the Supplementary Note.

Hi-C and UMI-4C. Hi-C and UMI-4C library preparation was performed as described in refs. [4,8,63], except for the GC cells, for which, due to the limited number of purified B cells obtained (~1×10^5), the Hi-C libraries were prepared using Arima-HiC (Arima Genomics), following the manufacturer's protocol. For all the other samples, two million cells were fixed in 2% formaldehyde solution (AppliChem, catalog no. UN2209), and the reaction was quenched with 2 µM glycine (VWR Chemicals, catalog no. 101196X). Cells were incubated in lysis buffer (10 mM Tris-HCl, pH 8.0 (Invitrogen, Thermo Fisher Scientific, catalog no. 15568025), 10 mM NaCl (Sigma-Aldrich, catalog no. 59222C), 0.2% IGEPAL CA-630 (Sigma-Aldrich, catalog no. I8896), 1× cOmplete Protease Inhibitor Cocktail (Sigma-Aldrich, catalog no. 11697498001)) for 30 min at 4 °C. The nuclei were spun down, resuspended in NEB3.1 buffer (New England Biolabs, catalog no. B7203S) and 0.1% sodium dodecylsulfate (SDS; Carl Roth, catalog no. CN30) final concentration, and incubated at 65 °C for 10 min. The SDS was quenched by the addition of 1% Triton X-100 (AppliChem, catalog no. A1388). The chromatin was then digested with 100 U of restriction endonuclease MboI (New England Biolabs, catalog no. R0147) overnight at 37 °C. Digested fragments were filled in with 0.4 mM biotin (Invitrogen, Thermo Fisher Scientific, catalog no. 19524016), 10 mM dCTP, 10 mM dGTP, 10 mM TTP (Promega, catalog no. U1330) using 50 U µl^{-1} of DNA polymerase I, large Klenow fragment (New England Biolabs, catalog no. M0210) and incubated at room temperature for 4 h. Proximity ligation of the biotin-filled ends was performed by the addition of 5 U µl^{-1} of T4 DNA Ligase (Thermo Fisher Scientific, catalog no. EL0011), 0.5× bovine serum albumin (New England Biolabs, catalog no. B9000S) and 1% Triton X-100 to the samples, which were incubated at room temperature for an additional 4 h. Crosslinks were reversed by treatment with 300 mM NaCl and 1% SDS overnight at 68 °C. Samples were treated with 50 µg ml^{-1} of RNase A (Thermo Fisher Scientific, catalog no. EN0531) for 30 min at 37 °C, followed by incubation with 400 µg ml^{-1} of proteinase K (Promega, catalog no. V3021) at 65 °C for 1 h. DNA was precipitated with 1.6× volumes of 100% ethanol and 0.1× volume of 3 M sodium acetate, pH 5.2 (Thermo Fisher Scientific, catalog no. R1181) and incubation at −80 °C for 1 h. DNA was purified with 70% ethanol and fragmented by sonication (Covaris E220). DNA was double size selected with 0.575×, followed by 1.2×, volumes of Ampure XP beads (Beckman Coulter, catalog no. A6388) to obtain fragments sizes of 300–700 bp.

Biotin-bound fragments were isolated on Dynabeads MyOne Streptavidin T1 beads (Thermo Fisher Scientific, catalog no. 65602) by incubation in binding buffer (10 mM Tris-HCl, pH 7.5 (Thermo Fisher Scientific, catalog no. 15567027), 1 mM ethylenediaminetetraacetic acid (Invitrogen, Thermo Fisher Scientific, catalog no. AM9260G), 2 M NaCl) for 30 min at room temperature. After biotin pull-down, the Hi-C and UMI-4C library preparation steps diverge. For Hi-C, bead-bound DNA is subjected to end polishing though the addition of 25 mM each of a dNTP mix (Thermo Fisher Scientific, catalog no. R1122), 3 U µl^{-1} of T4 DNA polymerase (New England Biolabs, catalog no. M0203S), 5 U µl^{-1} of DNA polymerase I, large Klenow fragment (New England Biolabs, catalog no. M0210L), 10 U µl^{-1} of T4 polynucleotide kinase (New England Biolabs, catalog no. M0201L) in 1× T4 DNA ligase reaction buffer (New England Biolabs, catalog no. B0202S), and incubation for 30 min at room temperature. The dA tail was added to the fragments by incubation with 10 mM dATP (Promega, catalog no. U1330) and 5 U µl^{-1} of Klenow fragment 3′→5′ exonuclease (New England Biolabs, catalog no. M0212L) for 30 min at 37 °C. Illumina Indexed TruSeq adapters were ligated to the DNA fragments with T4 DNA ligase and incubated at room temperature for 2 h. Finally, the bead-bound libraries were amplified using KAPA HiFi HotStart ReadyMix PCR Kit (KAPA Biosystems, catalog no. KK2600), and universal Illumina forward and reverse primers (Supplementary Table 7). Libraries were purified with 1.8× volumes of Ampure XP beads and subjected to pair-end sequencing, 2 × 150 bp, on the Illumina NovaSeq 6000 or NextSeq 500.

For UMI-4C, DNA fragment ends were repaired by incubation at room temperature for 30 min with 25 mM each of the dNTP mix, 3 U µl^{-1} of T4 DNA polymerase, 5 U µl^{-1} of DNA polymerase I, large Klenow fragment in 1× T4 DNA ligase reaction buffer. Repaired fragments were subjected to poly(A)-tail addition by mixing the sample with 10 mM dATP and 5 U µl^{-1} of Klenow fragment 3′→5′ exonuclease and incubation at 37 °C for 30 min. Exonuclease activity was stopped by heat inactivation at 75 °C for 20 min and 5′-end dephosphorylation was performed by treatment with calf intestinal alkaline phosphatase (New England Biolabs, catalog no. M0290) for 1 h at 50 °C. Ligation of Illumina Indexed TruSeq adapters was achieved with T4 DNA ligase and incubated at room temperature for 2 h. DNA libraries were obtained using a nested PCR amplification approach. Two types of primers were designed: downstream (DS) primers located at loci of interest, 5–15 bp away from the MboI restriction site, and primers located upstream to the DS primers. Multiple viewpoints were selected for primer design at each locus (Supplementary Table 7). For the first PCR reaction, bead-bound DNA was amplified for 10–16 cycles using KAPA HiFi HotStart ReadyMix PCR Kit, a 10-µM mix of all US viewpoints and 10 µM Illumina universal reverse primer. The output was cleaned up with 1.8× volumes of Ampure XP beads and subjected to the second PCR reaction. DNA was mixed with KAPA HiFi HotStart ReadyMix, a 10-µM mix of all DS primers and 10 µM Illumina universal reverse primer, and amplified for 10 cycles. Final libraries were purified with 1.8× volumes of Ampure XP beads and pair-end sequenced, 2 × 75 bp, on the Illumina NextSeq 500 or HiSeq4000 platforms.

ChIP–seq. Detailed description of the ChIP–seq sample preparation, analyses, peaks and enhancer regions calling are reported in the Supplementary Note.

Chromatin conformation capture analyses. *Processing of Hi-C data.* Four replicates for WSU-DLCL2 and four for Karpas-422, treated with A-485 for 48 h, were generated. The sequencing data were processed as previously described[4]. Briefly, for each library replicate, coordinate-sorted (SAMtools v.1.6) and PCR duplicate (Picard tools v.2.5.0)-cleaned bamfiles were generated after alignment of the reads to the human hg19 reference genome (Bowtie v.2–2.2.9) and filtering for uniquely mapping reads (SAMtools v.1.6). Custom Python and R scripts were used to process chimeric pairs with 'unambiguous' reads, for which one of the two reads mapped to two different subsequences. Those were recovered in a second round of alignment using bwa mem v.0.7.12 and processed as above. Read pairs from each replicate were binned in 20-kb windows to give one matrix of interactions per sample. Normalized matrices were generated using ICE normalization from HiC-pro[64].

Compartment calling. Hi-C contact maps binned at 40 kb were analyzed using the Calder algorithm[28]. Briefly, Calder computes a similarity measure between each pair of bins of the Hi-C map based on Fisher's z-transformed correlations of whole-chromosome interactions. Each chromosome is then partitioned into compartment domains, defined as a DNA region with high intraregion similarity and low similarity with adjacent regions. Compartment domains are then hierarchically clustered based on interdomain interactions and independently of linear proximity (that is, proximity along the genome sequence). Hierarchy branches are internally reordered, without disrupting the clustering structure, to match subcompartments among different chromosomes. Finally, a normalized rank value is assigned to each domain (between 0 and 1), to identify its position within the dendrogram. Domain ranks are correlated with histone mark intensities and A/B compartment classification[28]. Normalized rank values close to 0 indicate domains in the B compartment, whereas those close to 1 indicate domains in the A compartment. The classification in eight compartments was generated by cutting the domain hierarchy at the third level of the dendrogram, starting from the top (the hierarchy is built as a binary tree).

Comparisons of MER status in different cell lines. Representative MERs ($n = 1{,}644$) defined as described in the Supplementary Note were compared among GM12878, GC cells, Karpas-422 and WSU-DLCL2 based on their levels of H3K27ac and compartment domain ranks (Fig. 1 and Extended Data Fig. 1). To each MER a compartment domain rank was assigned based on the rank of the compartment domain in which the MER was located. The repositioning (Δposition or Δcompartment rank) of a domain between two cell lines was simply computed as the difference of the domain ranks assigned to that domain in the two cell lines. ΔH3K27ac was computed as the difference of mean H3K27ac observed at that MER in the cell lines compared. For scatterplot comparisons of Δcompartment ranks and ΔH3K27ac (Fig. 1c and Extended Data Fig. 1d,f,g), we considered only MERs in which H3K27ac was >0 in at least one of the two cell lines being compared and, for each cell line, we normalized non-0 H3K27ac values to range between 0 and 1. In this way, Δcompartment ranks and ΔH3K27ac are in the same (−1,1) range.

To compute the correlation between Δcompartment ranks and ΔH3K27ac (Extended Data Fig. 1e), for each pair of cell lines with, respectively, $k1$ and $k2$ numbers of MERs with H3K27ac >0 in one cell line and H3K27ac = 0 in the other cell line, we computed 100 correlation values by subsampling k MERs from the cell line with the largest between $k1$ and $k2$ such that $k = \min(k1, k2)$. In this way, each cell line had the same number of non-0 MERs. The same procedure was applied to compute the R_{90} radius (that is, the radius of the circle comprising 90% of points in the scatterplot—Extended Data Fig. 1d) and to compute MER correlations after random permutation of the MER labels. Correlation values observed and expected by randomization distributions are shown in Extended Data Fig. 1e.

Repositioning events in Fig. 1d–f were selected as the intersection between repositioning events with Δposition >0.4 or <−0.4 in the comparisons of Karpas-422 versus GM12878 and WSL-DLCL2 versus GM12878. The threshold of 0.4 was chosen to select the top ~10% repositioning events in these comparisons. Overlap of repositioning events and Fisher's test (Extended Data Fig. 1h,j) were performed, considering as universal MERs in which the ΔH3K27ac and Δposition were not 0.

Hi-C significant interactions. We used HiC-DC[38] to compute the statistical significance of chromatin interactions at bin level (20-kb resolution). Hi-C paired-end reads were mapped to the hg19 reference genome as described in previous sections. The degree of freedom in the hurdle negative binomial regression model was set as 6. We determined the sample size parameter by trying 20 values in the (0.5,1) range with equal distance, choosing the maximum value that did not result in optimization failure in R. Other parameters of HiC-DC were set as default.

We observed that the interaction P values resulting from HiC-DC were systematically lower for Hi-C datasets with a higher number of paired-end reads. To correct for this bias, we conducted chromosome-wise downsampling of paired-end reads within each comparison group included in our differential interactome analysis, such that each chromosome had the same number of paired-end reads in the data group. We defined four groups for different comparisons: group 1: GM12878, K562, Karpas-422, WSU-DLCL2 and GC; group 2: WSU-DLCL2 before and after A-485 treatment; group 3: Karpas-422 before and after A-485 treatment; and group 4: GM12878, GC, patients 1 and 7. The downsampling vectors used in each analysis are provided in Supplementary Table 2.

EPIs and differential EPI analysis (DiffInt). Significant EPIs were determined as a subset of significant HiC-DC interactions. For this analysis, we tested interactions between each of the 1,644 representative MERs and gene promoters that were found at a maximum distance of 2 Mb from each MER. Precisely, for each enhancer, we considered HiC-DC nominal P values in a rectangle of $m \times 2$ pixels, where m is the number of bins encompassing the enhancer region and two bins were considered for each promoter, one corresponding to the locus of the transcription start site and a second adjacent one selected in the direction of the enhancer to capture a broader signal. For each EPI, we kept track of the minimal P value in the $m \times 2$ rectangle and the number of pixels with $P < 0.001$. An EPI was considered significant when at least one pixel had a P value < 0.001. The percentage of significant EPIs falling within the same compartment domain (observed) was compared with its expected value, defined by the overall percentage of candidate EPIs that fell within the same compartment domain (Extended Data Fig. 2b). For a given pair of cell lines or two conditions of the same cell line, differential interaction analysis (DiffInt) was performed among all pairs of EPIs that were significant in at least one of the two cell lines/conditions being compared. The interaction strength S of each EPI was defined as the mean of $-\log_{10}$(transformed HiC-DC P values) in the $m \times 2$ rectangle. We then computed the difference of interaction strength between two cell lines/conditions as $\Delta S = S_1 - S_2$ and tested ΔS for significant deviation from 0 with respect to a background distribution. We generated the background distribution by computing ΔS for all possible $m \times 2$ rectangles within a 2-Mb window across all chromosomes. An empirical, two-tailed P value was obtained from this background distribution as $p = P(|\Delta S| > |\Delta S_{\text{background}}|)$. Significant differences were retained when $P < 0.05$. In each comparison, we also kept track of the 'direction' of the significant difference (−1 or 1), that is, whether a given EPI was found significantly more frequently in the cell line/condition 1 or 2. (For example, the direction of the DiffInt analysis is used to generate the barplots in Fig. 3c.) DiffInt in lymphoma cell lines before and after A-485 treatment was performed in a nonbiased fashion on all candidate EPIs, but then focused on EPIs that we previously found significantly more frequently in lymphoma cell lines than in GM12878 (lymphoma EPIs). Last, we compared the number and size of significantly different EPIs that were more frequent in lymphoma cell lines than in GM12878 or GC, as a function of the difference of H3K27ac at the enhancer region. We iteratively considered only EPIs such that the difference of H3K27ac between lymphoma cell lines and GM12878 or GC was >0, 0.1, 0.2, 0.3, 0.4, 0.5, 0.6 or 0.7. For each threshold, we computed the percentage of significantly different EPIs with direction = 1 (more frequent in lymphoma) and took the ratio between this value and the overall percentage of significantly different EPIs with direction = 1 (Fig. 2d and Extended Data Fig. 2d). Similarly, we defined the size of a given EPI as the number of pixels of the $m \times 2$ rectangle studied for each EPI that had an HiC-DC $P < 0.001$ (that is, number of significant pixels). For each ΔH3K27ac threshold defined above, we derived the mean EPI size of EPI with direction = 1.

Phasing sequencing reads of chr.8 and chr.18. To attribute the read to each copy of chr.8 in WSU-DLCL2, first single-nucleotide variants (SNVs) were identified from the WGS data by freebayes v.1.1.0–60-gc15b070 (https://github.com/ekg/freebayes) and phased into two haplotypes, namely hap1 and hap2, by Eagle v.2.4 (ref. [65]) using hg19 1000 Genomes project phase 3 as a reference panel. Details for WGS analyses and SNP calling can be found in the Supplementary Note. In a second step, HapCUT2 (ref. [66]) was used to resolve the haplotype of WSU-DLCL2 cell line from combined WGS and Hi-C data. Phased SNVs from step 1, which were missing from the haplotype blocks obtained from the read phasing in step 2, were added to the corresponding blocks. Those blocks were then used in the downstream analysis. To phase the reads on the chr.18 locus from Hi-C data in WSU-DLCL2 cells, we used a slightly different strategy to increase coverage. We first identified SNVs at the *BCL2* locus by considering the exclusive reads mapping the interaction between the translocated copy of chr.18 and chr.14. Then, pair-end reads for each allele containing an SNV were attributed to putative hap1 (the translocated chromosome copy) or hap2 (the WT copy) according to whether it is present on the majority (>50%) of the chr.18 reads. These phased SNVs were used to separate H3K27ac ChIP–seq, RNA-seq and Hi-C reads into hap1 or hap2. With this information, we built two haplotype-specific mini-Hi-C maps by extracting contacts with both the forward and reverse reads of the interaction pair coming from the same haplotype. For phasing ChIP–seq data of patient 1, SNVs were identified from the pooled reads of H3k27ac ChIP–seq data and Hi-C data using freebayes, and phased into hap1 and hap2 using Eagle as described previously.

UMI-4C data processing and UMI-4 and Hi-C phasing. The UMI-4C data for the different experiments were processed using 'umi4cPackage'[63] or 'UMI4Cats'[67] R packages implementing the same analysis pipeline. Unique molecular identifiers (UMIs) for the different replicates were pooled for each cell line and condition. To analyze chr.8–chr.3 interactions, read name and alignment coordinates, independent of the primer/bait of origin, supporting either chr.8–chr.8 or chr.8–chr.3 interactions, were obtained from the fendchain files. The read sequences were then extracted from the bamfiles produced by the umi4cPackage analysis and assigned to hap1 or hap2 blocks, based on the variants they exhibited. The reads, once assigned to a haplotype block, were further categorized as translocated if they were involved in a chr.8–chr.3 interaction. This allowed definition of variants and haplotype blocks from the translocated chromosome, and consequently variants and blocks belonging to the nontranslocated chromosome. Phasing of RNA-seq and ChIP–seq data is reported in the Supplementary Note.

Reporting Summary. Further information on research design is available in the Nature Research Reporting Summary linked to this article.

Data availability

RNA-seq and H3K27ac ChIP–seq data were obtained as follows: for lymphoblastoid cells from ref. [68] and the ArrayExpress Archive (http://www.ebi.ac.uk/arrayexpress), accession nos. E-MTAB-3656 and E-MTAB-3657, for GM12878 from ENCODE accession nos. GSE78551 and GSM733771, for SU-DHL-4, accession nos. GSM1227199 and GSM1703927, for OCI-LY7, accession nos. GSM1227199 and GSE86708, for DoHH2 ENCODE accession nos. GSM2366283 and GSE86743, for Karpas-422 accession no. GSE86733 (H3K27ac), for primary centrocytes and centroblasts, accession nos. GSE62246 and GSE89688, for five primary follicular lymphoma and two GC diffuse large B-cell lymphoma BLUEPRINT, accession no. EGAD00001001502. WGS data and RNA-seq data were obtained for lymphoma cell lines and for 30 primary DLBCLs and their matched controls from dbGaP (phs000235.v13.p2). WGS data and RNA-seq data for Burkitt's lymphoma or DLBCL with t(8;14) were downloaded from the Malignant Lymphoma MMML ICGC portal. RNA-seq data were generated for Karpas-422 and WSU-DLCL2 that were nontreated and treated by A-485 and for three independent clones WSU-DLCL2 with *BCL11A* knockout (data are deposited in the Gene Expression Omnibus database at accession no. GSE168471). CTCF ChIP–seq data were obtained from ENCODE for GM12878 and we generated the data for Karpas-422 and WSU-DLCL2 that were nontreated and treated by A-485 (accession no. GSE168470). H3K36me3 ChIP–seq data were generated for WSU-DLCL2 (accession no. GSE168472). Hi-C data for nontreated WSU-DLCL2 and Karpas-422 were obtained from Donaldson-Collier et al.[4] and generated for the treated replicates for the present study (accession no. GSE168470). Source data are provided with this paper.

Code availability

Code availability for Calder method: https://github.com/CSOgroup/CALDER.

References

58. Schwartzman, O. et al. UMI-4C for quantitative and targeted chromosomal contact profiling. *Nat. Methods* **13**, 685–691 (2016).
59. Servant, N. et al. HiC-Pro: an optimized and flexible pipeline for Hi-C data processing. *Genome Biol.* **16**, 259 (2015).
60. Loh, P.-R., Palamara, P. F. & Price, A. L. Fast and accurate long-range phasing in a UK Biobank cohort. *Nat. Genet.* **48**, 811–816 (2016).

61. Edge, P., Bafna, V. & Bansal, V. HapCUT2: robust and accurate haplotype assembly for diverse sequencing technologies. *Genome Res.* **27**, 801–812 (2017).
62. Ramos-Rodriguez, M. & Subirana-Granes, M. UMI4Cats: Processing, analysis and visualization of UMI-4C chromatin contact data. R package version 4.0 https://doi.org/10.18129/B9.bioc.UMI4Cats (2021).
63. Waszak, S. M. et al. Population variation and genetic control of modular chromatin architecture in humans. *Cell* **162**, 1039–1050 (2015).

Acknowledgements

We thank EPFL facilities and, in particular, B. Mangeat for the sequencing facility and M. Pujol for cell sorting at CIML. This work was supported by the ISREC Foundation (E.O.), the Swiss National Science Foundation (grant number 31003A_182526) (E.O.) and Swiss Cancer Research foundation (grant number KFS-3982-08-2016-R) (E.O.), and the Gelu Foundation. G.C. is supported by the Giorgi–Cavaglieri Foundation. S.R. is supported by the French National Cancer Institute (INCa) Epigenetic and Cancer program. S.S. has been supported with a Marie Curie EPFL fellow.

Author contributions

S.S. was involved in the experimental design. Y.L. developed a new method and analyzed Hi-C data. S.S. and Y.L. analyzed Hi-C, UMI-4C and ChIP–seq data, and performed the phasing analyses. M.D.C., R.L. and N.K. prepared Hi-C, UMI-4C, ChIP- and RNA-seq libraries, and performed all experimental validations. D.T. analyzed and normalized ChIP–seq data. S.R. obtained and sorted the germinal center cells and prepared cells for ChIP and Hi-C library preparation G.C. supervised the computational analyses. E.O. designed the study and wrote the manuscript, with comments from all authors.

Competing interests

The authors declare no competing interests.

Additional information

Extended data is available for this paper at https://doi.org/10.1038/s41588-021-00842-x.

Supplementary information The online version contains supplementary material available at https://doi.org/10.1038/s41588-021-00842-x.

Correspondence and requests for materials should be addressed to E.O.

Peer review information *Nature Genetics* thanks Berkley Gryder, Rolf Ohlsson and the other, anonymous, reviewer for their contribution to the peer review of this work. Peer reviewer reports are available.

Reprints and permissions information is available at www.nature.com/reprints.

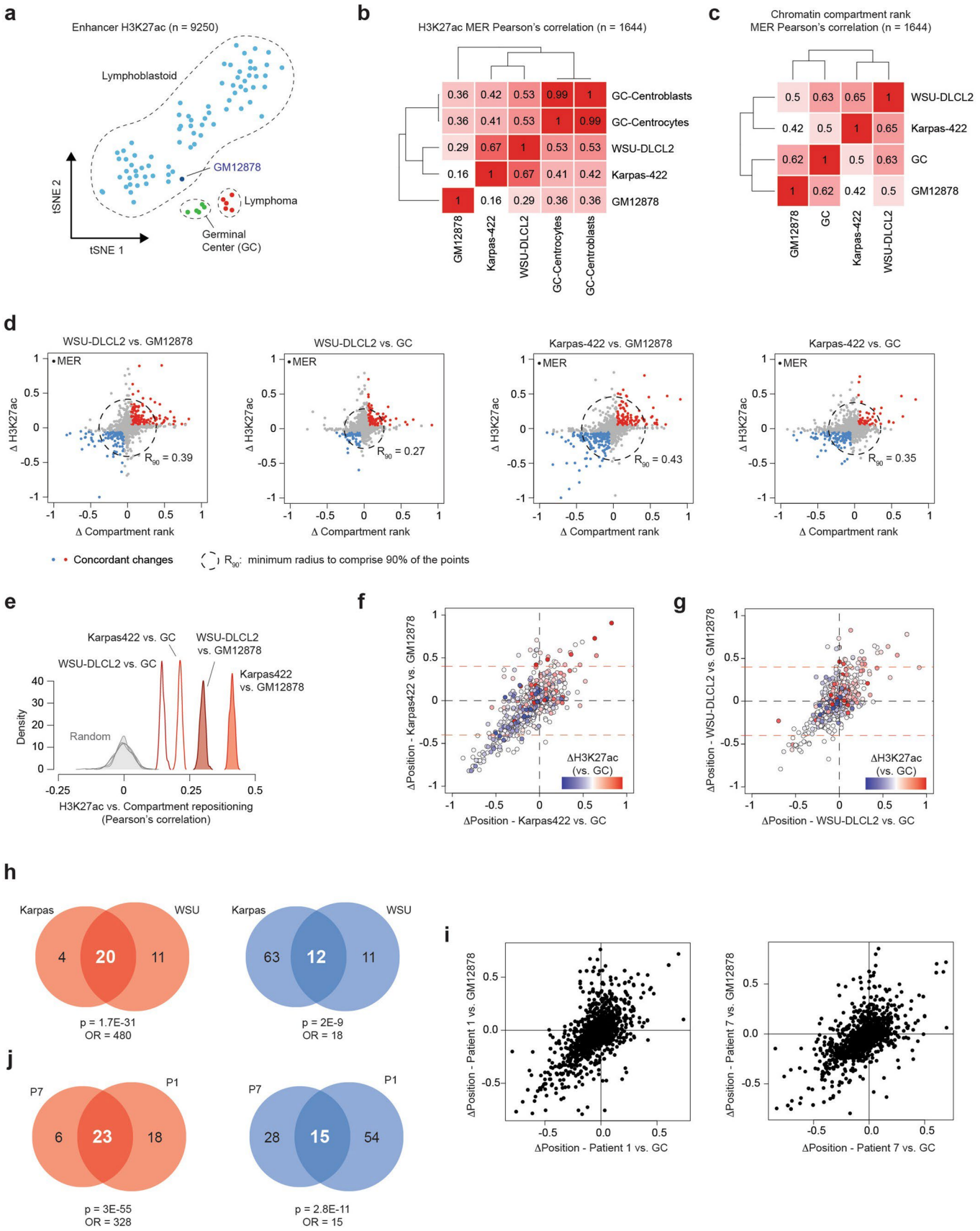

Extended Data Fig. 1 | See next page for caption.

Extended Data Fig. 1 | Genome-wide analyses of H3K27ac changes and chromatin sub-compartments. **a**. t-SNE plot based on the levels of H3K27ac in 9250 MERs in lymphoblastoid samples (n = 76, blue, GM12878 in dark blue), GC, (n = 5 green), and GC-DLBCL (n = 5, red). **b**. Heatmap and clustering of 5 cell lines based on the Pearson's correlation coefficients (values are indicated and color coded) between H3K27ac levels of MERs (n = 1644). **c**. Heatmap and clustering of 4 cell lines analyzed by Hi-C based on the Pearson's correlation coefficients (values are indicated and color coded) between compartment domain ranks of MERs (n = 1644). **d**. For each pair of cell lines a scatterplot comparison shows the difference of compartment domain ranks computed by CALDER (x-axis) and of H3K27ac levels (y-axis) computed for each enhancer region (dots). Enhancer regions exhibiting concordant changes are color-coded (red positive differences, $>5\%$, blue negative differences $<-5\%$). For each comparison, the radius of the circle comprising 90% of the points (R_{90}) is shown. **e**. For each comparison, Pearson's correlation coefficient (x-axis) between differences of compartment domain ranks and of H3K27ac. Distribution of correlation values (colored) are compared to expected distributions (gray). f-g. Comparison of compartment domain rank differences computed with CALDER between (f) Karpas-422 and GC cells (x-axis) and Karpas-422 and GM12878 (y-axis) and between (g) WSU-DLCL2 and GC cells (x-axis) and WSU-DLCL2 and GM12878 (y-axis). Each dot is a merged enhancer region color coded by the difference of H3K27ac between Karpas-422 (left) or WSU-DLCL2 (right) and GC **h**. Overlap of repositioned enhancer regions towards a more active (red) or inactive (blue) sub-compartments in Karpas-422 and WSU-DLCL2 cells with respect to GM12878. P-values and odds-ratio (OR) were computed by two-sided Fisher's exact test. **i**. Comparison of compartment domain rank differences computed with CALDER between (left) Patient 1 and GC cells (x-axis) and Patient 1 and GM12878 (y-axis) and between (right) Patient 7 and GC cells (x-axis) and Patient 7 and GM12878 (y-axis). **j**. Overlap of repositioned enhancer regions towards a more active (red) or inactive (blue) sub-compartments in Patient 1 and Patient 7 with respect to GM12878. P-values and odds-ratio (OR) were computed by two-sided Fisher's exact test.

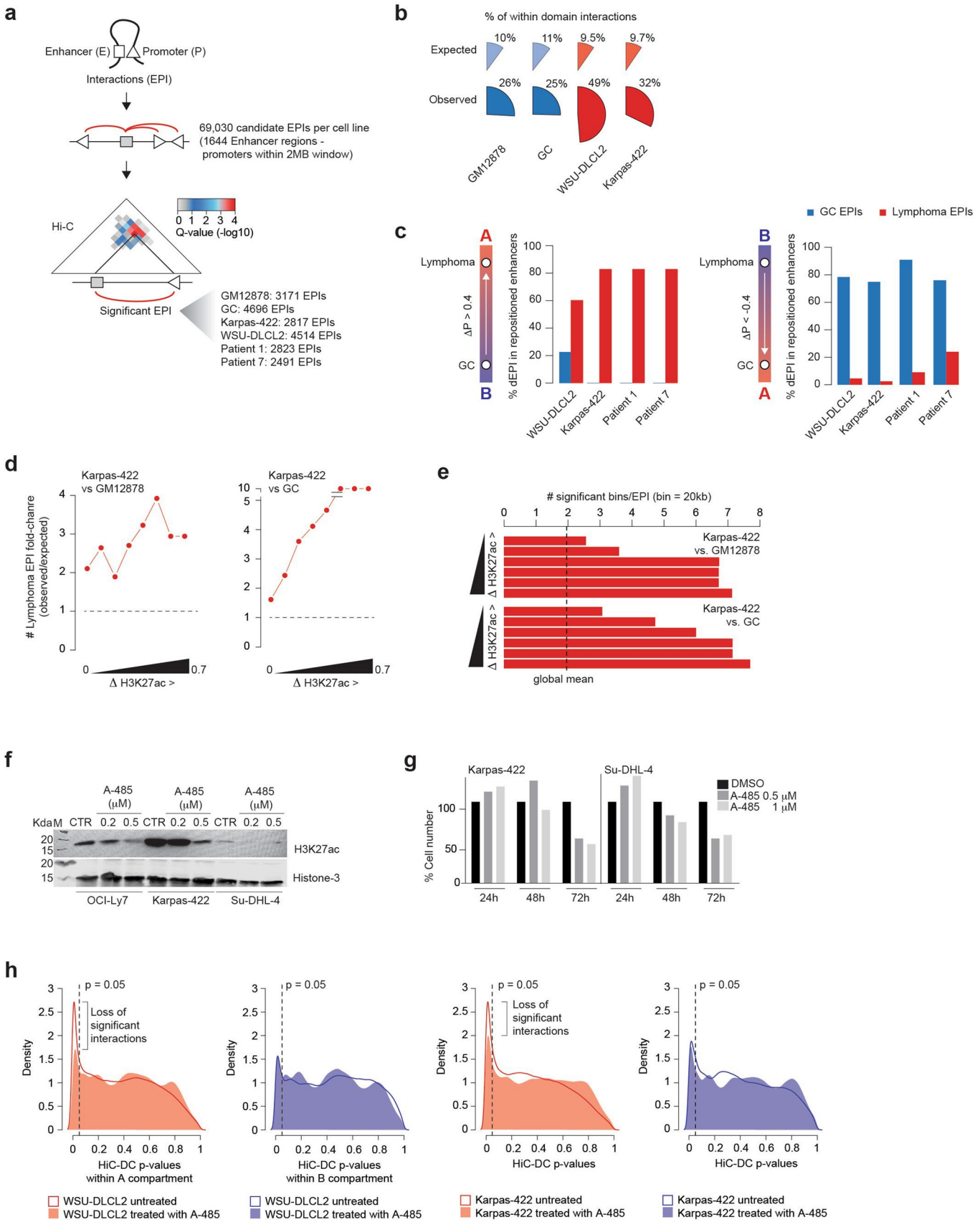

Extended Data Fig. 2 | See next page for caption.

Extended Data Fig. 2 | Genome wide analyses of enhancer promoter interactions (EPIs) and changes in H3K27ac. **a**. Graphical representation of enhancer-promoter interactions (EPIs, top) analysis. The total number of tested and significant EPIs is reported for each cell line. **b**. Fraction of significant EPI that are expected (top) and that were observed (bottom) to occur between enhancers and promoters within the same compartment domain. **c**. Percentage of significantly different EPIs (y-axis) which are more frequent either in GC than in the indicated lymphoma samples (blue bars) or in lymphoma samples than in GC (red bars). Results are shown for enhancer regions that were repositioned from inactive to active compartment (left) or from active to inactive compartment (right) in lymphoma samples with respect to GC. **d**. Fold-change between the observed and expected number of significantly more frequent EPIs (y-axis) in Karpas-422 than in GM12878 (left) and in GC (right) with respect to the difference in H3K27ac in these regions. **e**. Number of significant interactions per EPI (that is, number of bins of the Hi-C map with significantly frequent interactions between the enhancer and promoter regions) (x-axis) with respect to the difference in H3K27ac in these regions. Results are shown for EPIs that were more frequent in Karpas-422 than in GM12878 (top) or in GC (bottom). **f**. Representative western blot image (n=2 independent experiments) detecting the H3K27ac and histone-3 treated with DMSO (vehicle) or 0.2 μM and 0.5 μM A-485 for 48h in the indicated lymphoma cell lines. **g**. Quantification of cell survival of Karpas-422 and Su-DHL-4 cells treated with 0.5 μM and 1μM A-485 or DMSO. **h**. Density plot of the p-values inferred by HiC-DC for each interaction in WSU-DLCL2 and Karpas-422 Hi-C maps connecting bins at most 2 Mb apart. P-values below 0.05 (left of black dashed line) indicate significant contacts.

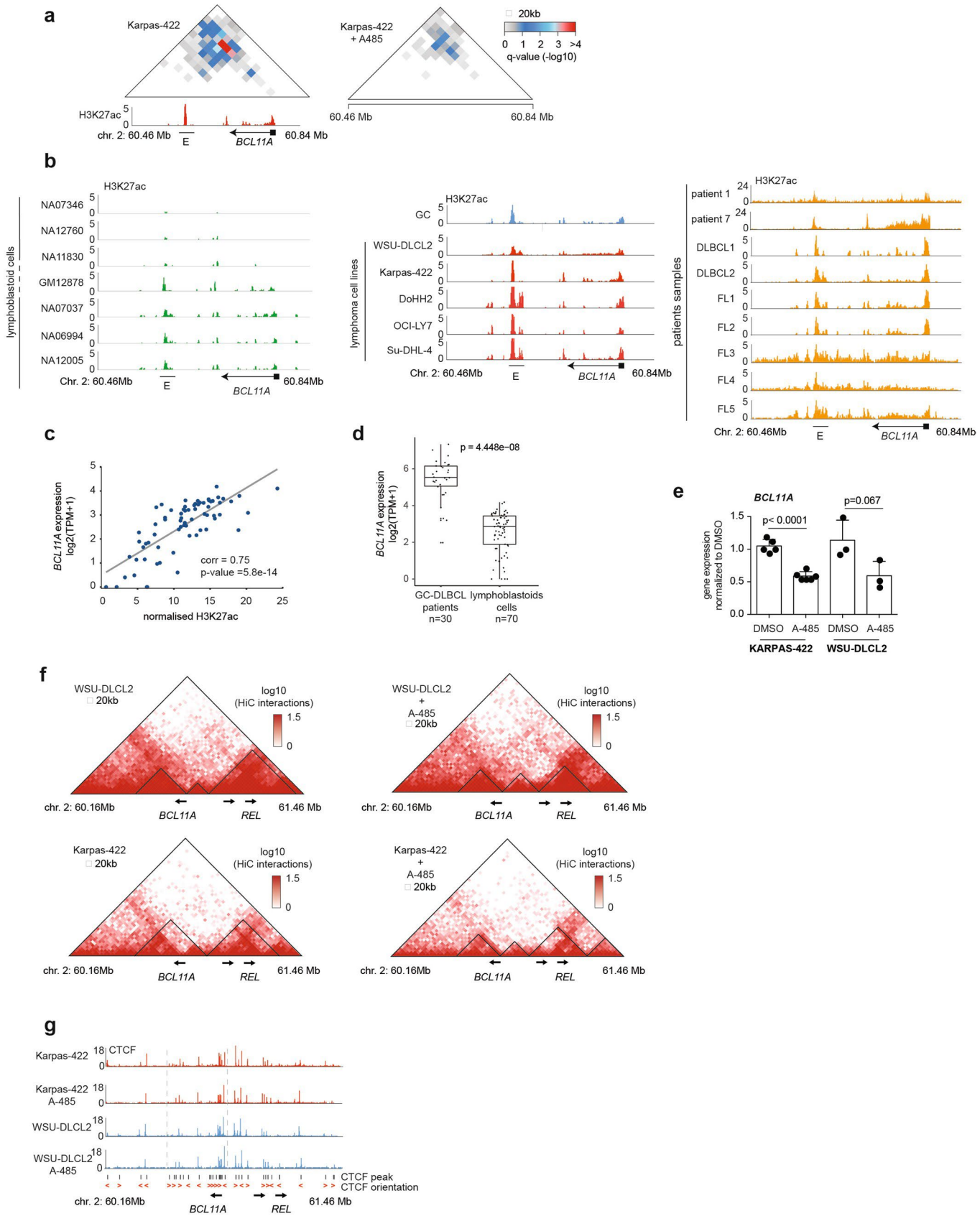

Extended Data Fig. 3 | See next page for caption.

Extended Data Fig. 3 | Chromatin conformation analyses of *BCL11A* region upon pharmacological depletion of H3K27ac. **a**. Representation of 20kb interacting regions on chr.2: 60.46–60–86 Mb color coded based on their q-value in Karpas-422 cells untreated and treated with A-485 inhibitor (top) and corresponding ChIP-sequencing track of H3K27ac (NRPM) (botton). **b**. Representative H3K27ac ChIP sequencing tracks for the indicated genomic locus of lymphoblastoid samples, GC, lymphoma cells and lymphoma patients (NRPM). Patient 1 and Patient 7 are reported as RRPM x 10^{-2}. **c**. Spearman correlation plot of H3K27ac levels and *BCL11A* expression in 70 lymphoblastoid samples. two-tailed p value is calculated from the t-statistics of the corresponding correlation value. **d**. *BCL11A* expression levels in GC-DLBCL patients (n=30) and lymphoblastoid cells (n=70). The thick central line of each box plot represents the median expression value, the bounding box corresponds to the 25th–75th percentiles, and the whiskers extend up to 1.5 times the interquartile range. p-value was calculated with two tailed t-test. **e**. Quantification of expression changes of *BCL11A* upon treatment with A-485 0.5 μM for 48h in Karpas-422 (n= 6) and WSU-DLCL2 (n= 3) compared to the same cells treated with DMSO (vehicle Karpas-422 n= 5 and WSU-DLCL2 n=3). The black dots represent the number of independent experiments. Data are presented as mean value + SD. p-value were calculated using unpaired two-tailed t-test **f**. Hi-C contact maps of chr.2: 60.16–61.46 Mb region in Karpas-422 and WSU-DLCL2 cells untreated and treated with A-485. The lines in black delineate the compartment domains. The position of relevant genes is indicated. **g**. CTCF ChiP-seq tracks of chr.2: 60.16–61.46 Mb region in Karpas-422 and WSU-DLCL2 treated and untreated with A-485 (RPM). The detection of CTCF and their orientation is reported.

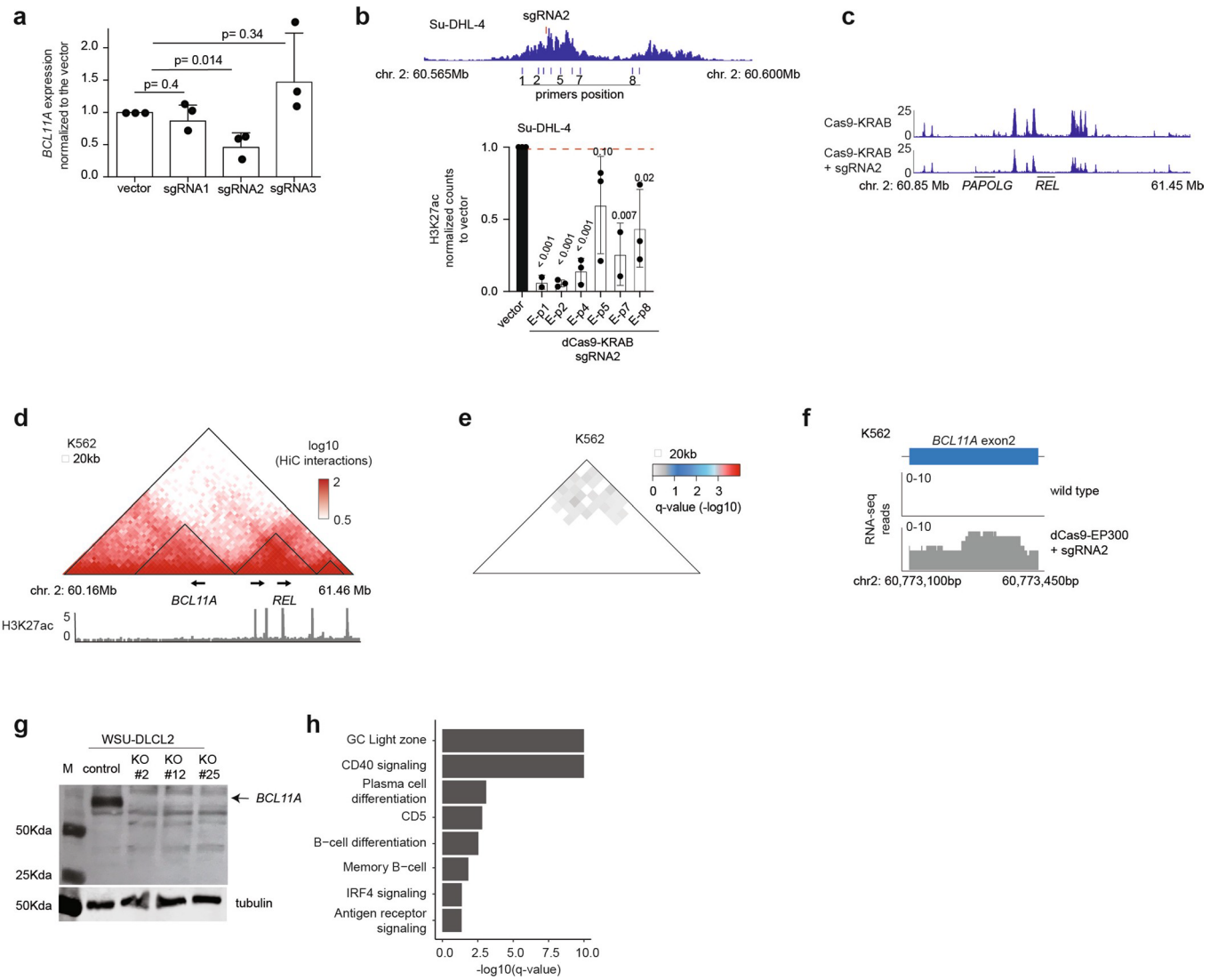

Extended Data Fig. 4 | Chromatin conformation analyses of *BCL11A* region upon genetic modification of H3K27ac. **a**. Quantification of *BCL11A* expression changes in Su-DHL-4 cells expressing dCas9-KRAB-sgRNA1, dCas9-KRAB-sgRNA2, dCas9-KRAB-sgRNA3 compared to cells expressing dCas9-KRAB. n=3 independent biological replicates. Data are presented as mean value + SD p-value were calculated by unpaired two-tailed t-test. **b**. H3K27ac ChIP sequencing tracks in Su-DHL-4 labelled with the position of the primers used for ChIP-qPCR and quantification of H3K27ac by ChIP-qPCR with the indicated primers. n=3 independent biological replicates. Data are presented as mean value ± SD. p-value were calculated by unpaired two-tailed t-test **c**. H3K27ac ChIP sequencing tracks in Su-DHL-4 on the regions on chr.2 (60.85–61.45 Mb) flanking the *BCL11A* region (RRPM x10^{-3}). **d**. Hi-C contact map and ChIP sequencing track of H3K27ac (RPM) in K562 cells in the indicated genomic region. **e**. Representation of 20kb interacting regions on chr.2: 60.46–60–86 Mb color coded based on their q value in K562 cells. **f**. Representation of the number of reads spanning *BCL11A* exon2 detected by RNA-sequencing in K562 cells expressing dCas9-EP300 and dCas9-EP300-sgRNA2. **g**. Representative western-blot image (n=2) of BCL11A and tubulin in WSU-DLCL2 cells (control) and three independent *BCL11A* knock-out clones (KO#2, KO#12, KO#25). **h**. Bar plot of the representative gene set enriched categories that significantly scored.

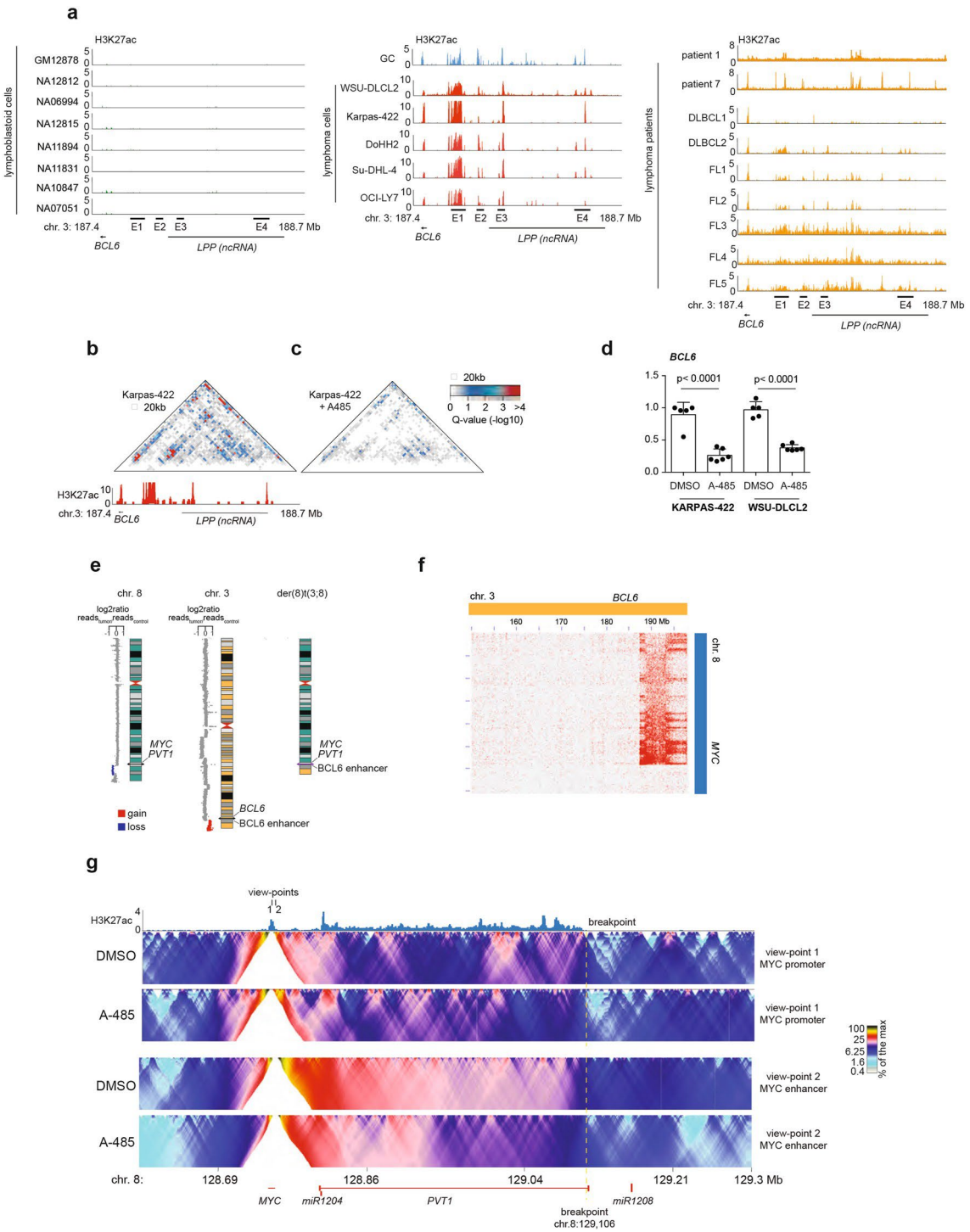

Extended Data Fig. 5 | Analyses of the chromatin structure in *BCL6* and *MYC* loci. **a**. Representative ChIP sequencing tracks of H3K27ac in lymphoblastoid cells, GC, DLBCL tumor cells, and in primarylymphoma samples (NRPM), Patient 1 and Patient 7 are reported as RRPM x10^{-2}. b-c. Representation of 20kb interacting regions in chr.3 187.4–188.7 Mb color coded based on their q value (top) in Karpas-422 untreated (**b**) or treated with A-485 inhibitor (**c**) and corresponding H3K27ac ChIP-sequencing (NRPM). **d**. Quantification of expression changes of *BCL6* upon treatment with A-485 0.5 µM for 48h in Karpas-422 (n=6) and WSU-DLCL2 (n=6) compared to the same cells treated with DMSO (vehicle, n=5). The black dots represent the number of independent experiments. Data are presented as mean value + SD. p-value were calculated using unpaired two-tailed t-test. **e**. Representation of copy number changes detected on chr. 8 and chr. 3 and graphical representation of the derivative chromosome t(3;8). **f**. Hi-C inter-chromosomal contact maps of chr.8 and chr.3 in the region spanning the breakpoint in WSU-DLCL2 cells. **g**. ChIP-sequencing track of H3K27ac (blue, NRPM) and UMI-4C domainogram with two different bait-primers representing the mean number of contacts (% of the maximum) on chr.8 spanning the breakpoint in WSU-DLCL2 cells treated with A-485 (0.5 µM for 48h) or DMSO as control.

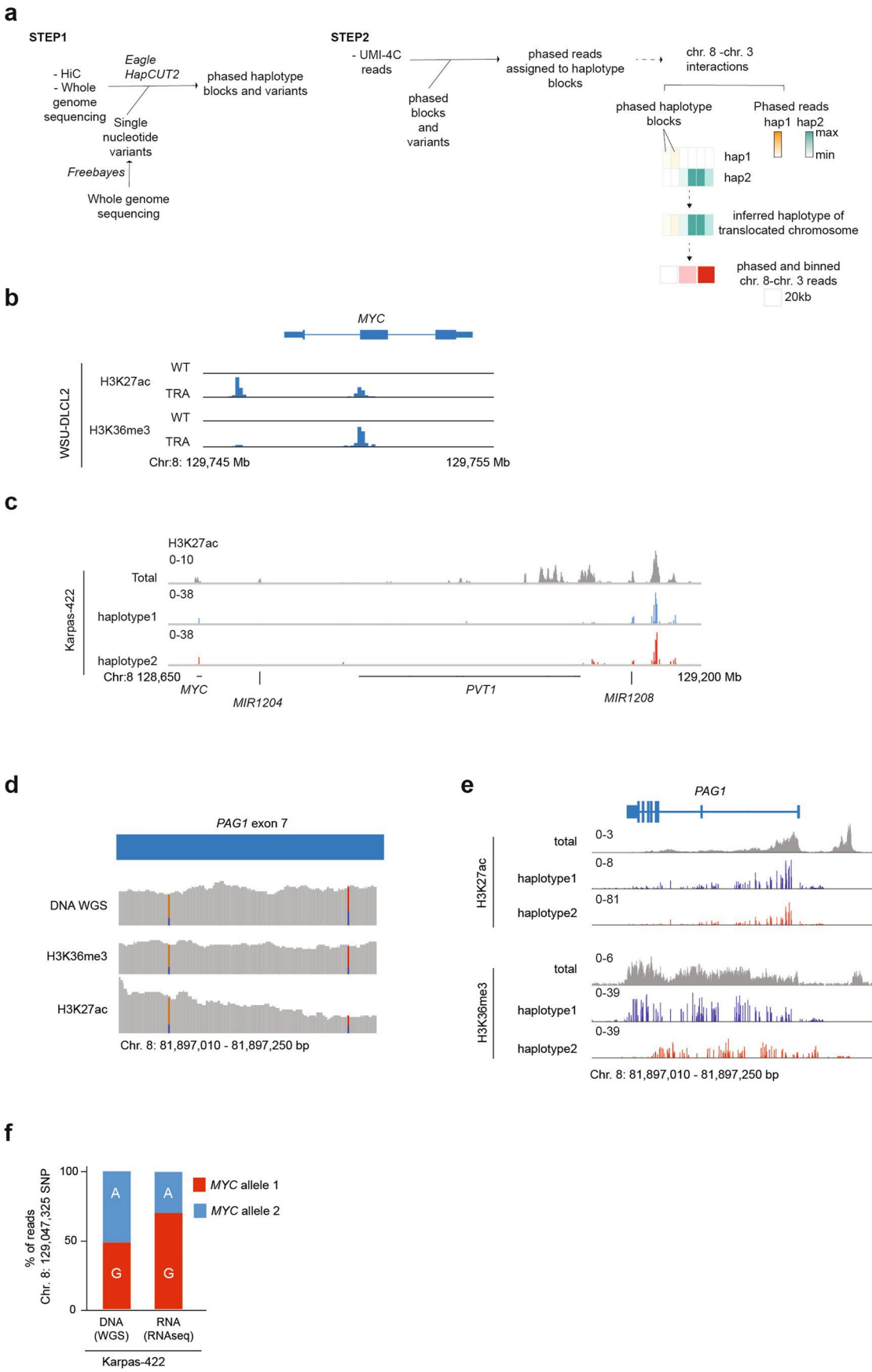

Extended Data Fig. 6 | See next page for caption.

Extended Data Fig. 6 | Epigenetic marks distributed to each copy of chromosome 8 based on their haplotype. **a**. Schematic representation of the phasing protocol used to define the haplotypes of the two copies of chr. 8. **b**.H3K27ac and H3K36me3 signal distribution in wild-type (WT) and translocated chromosome (TRA) in WSU-DLCL2 cells between chr.8:128,745–128,755 Mb region **c**. H3K27ac ChIP tracks of chr.8 indicated region in Karpas-422. In grey the total number of reads, in blue the number of reads with SNPs mapping on the haplotype 1 and red the number of reads with SNPs mapping on the haplotype 2 (NRPM). **d**. Representation of the reads distribution in whole genome sequencing (WGS), H3K27ac and H3K36me3 ChIP sequencing in the indicated genomic regions. In grey, genomic positions without detected SNPs and in two color bars genomic position with detected SNPs. **e**. H3K27ac and H3K36me3 ChIP tracks in the chr.8 indicated region (NRPM). In grey the total number of reads, in blue the reads with SNPs mapping on the haplotype 1 and red the number of reads with SNPs mapping on the haplotype 2. **f**. Quantification of the number of reads spanning the chr8:129,047,325 SNP harboring an adenine (A) or a guanine (G) detected by whole genome sequencing (WGS) and RNA- sequencing (RNA-seq) in Karpas-422 cells.

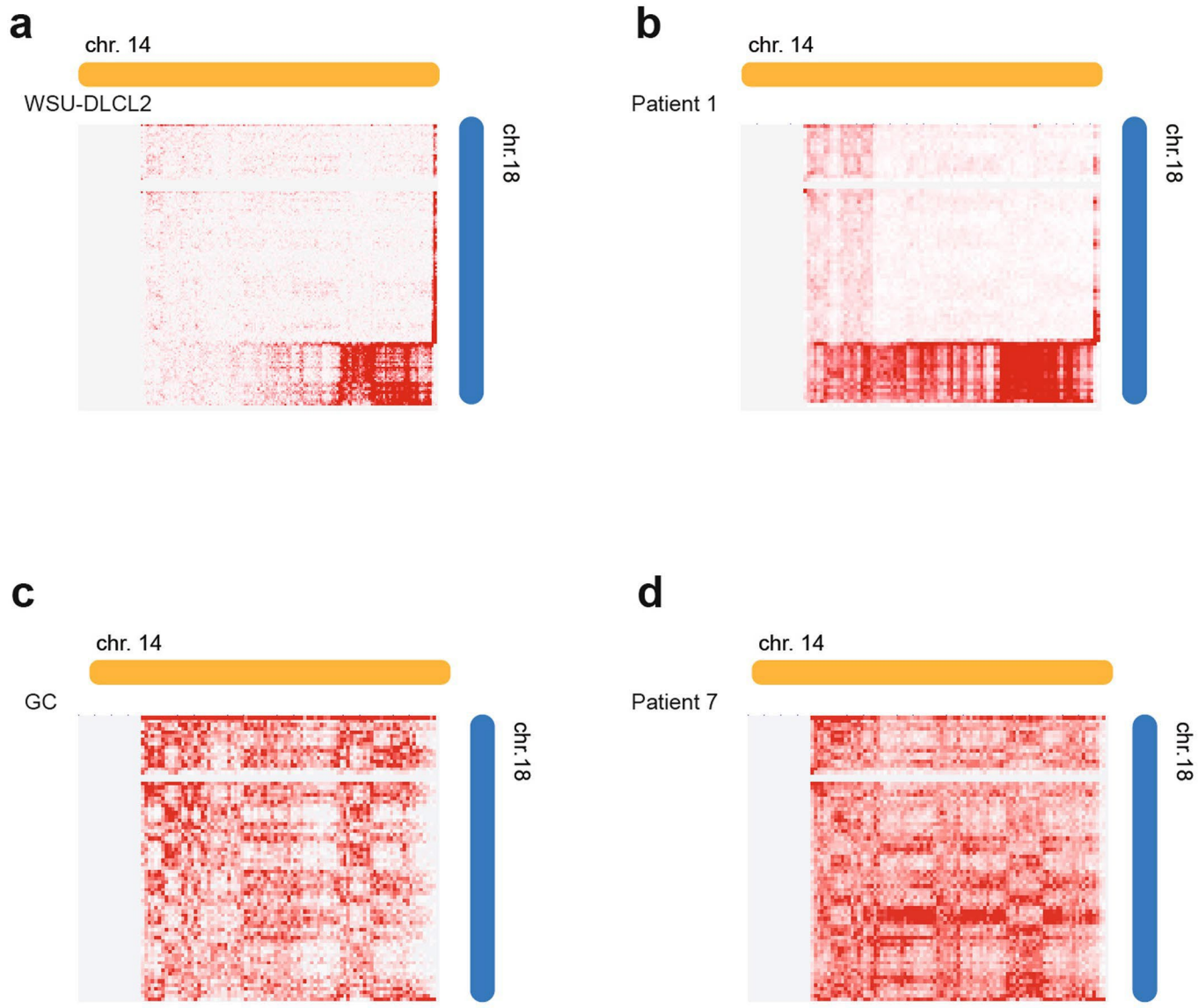

Extended Data Fig. 7 | Chr.14–18 inter-chromosomal interactions in samples with and without translocation. a-d. Hi-C inter-chromosomal contact maps of chr.14 and chr.18 in the region spanning the breakpoint in WSU-DLCL2 cells (**a**), Patient 1(**b**), GC (**c**) and Patient 7 (**d**).